PONTIFICAL CATHOLIC UNIVERSITY OF PARANA
MECHANICAL ENGINEERING GRADUATE PROGRAM

LUCIANO AYRES DE MELLO

ADVANCED MODELING OF HEAT, AIR AND MOISTURE (HAM) TRANSFER THROUGH POROUS BUILDING ELEMENTS

Curitiba
November 2017

PONTIFICAL CATHOLIC UNIVERSITY OF PARANA
MECHANICAL ENGINEERING GRADUATE PROGRAM

LUCIANO AYRES DE MELLO

ADVANCED MODELING OF HEAT, AIR AND MOISTURE (HAM) TRANSFER THROUGH POROUS BUILDING ELEMENTS

Ph.D. Thesis submitted as a qualifying examination in partial fulfillment of the requirements for the degree of Doctor of Mechanical Engineering of the Pontifical Catholic University of Parana.

Area: Engineering and Thermal Sciences

Supervisor: Luís Mauro Moura
Co-supervisor: Nathan Mendes

Curitiba
November 2017

Mello, Luciano Ayres de

M527a 2017 Advanced modeling of heat, air and moisture (HAM) transfer through porous building elements / Luciano Ayres de Mello ; supervisor: Luís Mauro Moura ; co-supervisor, Nathan Mendes. -- 2017

57 f. : il. ; 30 cm

Tese (doutorado) – Pontifícia Universidade Católica do Paraná, Curitiba, 2017.

Bibliografia: f. 52-57

1. Engenharia mecânica. 2. Solos – Umidade. 3. Calor – Transmissão. 4. Modelos matemáticos. 5. Algoritmos. I. Moura, Luís Mauro. II. Mendes, Nathan. II. Pontifícia Universidade Católica do Paraná. Programa de Pós-Graduação em Engenharia Mecânica. III. Título.

CDD 20. ed. – 620.1

Dados da Catalogação na Publicação
Pontifícia Universidade Católica do Paraná
Sistema Integrado de Bibliotecas – SIBI/PUCPR
Biblioteca Central
Edilene de Oliveira dos Santos -CRB9/1636

Abstract

Insulation porous structures have a significant role in building energy and hygrothermal performance. However, most of the mathematical models used in building simulation codes simplify the three heat transfer modes and, rarely, consider the moisture transport and, even more rarely, combine conductive and radiative transfer modes through multi-layered insulated envelopes or coupled multidimensional heat and moisture diffusion phenomena with detailed solution of surrounding airflow. In this way, first presents the governing equations based on temperature and vapor pressure gradients as driving potentials and includes radiation - not only as a boundary condition but also as heat transfer mode through participating fibrous media. The main objective is proposed model's validate with comparisons to the well done cases solved in the literature. The energy and moisture equations are solved using a fully implicit scheme and MTDMA algorithm to calculate the heat, air and moisture (HAM) fluxes through porous building elements containing fibrous materials such as glass wool. This new model called CAR-HAM (Conductive, Advective, and Radiative Heat, Air and Moisture) is verified with the HAMSTAD benchmark - including rain load in the analysis of moisture and temperature profiles - and with literature data for heat transfer through insulated roofs. Then the CAR-HAM model has been written to be fully coupled and solved by means of the CFD algorithm/solver available in ANSYS-Fluent, enabling also to calculate multidimensional distributions of moisture and temperature within porous structures. This second model called CFD-HAM is mainly applied to solve cases in two - and three - dimensions. The interactions between building porous elements and indoor and outdoor air are fully and straightforwardly coupled considering the Navier-Stokes equations to simulate both structure and air domains. Local values for mass and heat transfer convective coefficients are also obtained by the CFD simulation for a more accurate assessments of moisture content and temperature distributions within porous building elements of any geometric. The result of the model had a good agreement with the literature data. The mathematical model present an efficient algorithm enable to solve several problems related to the distribution of heat, humidity and temperature.

***Keywords**: Hygrothermal performance, insulation material, multidimensional Heat, Air and Moisture Transfer, moisture, HAM, CFD-HAM.*

Acknowledgments

This work is the result of a significant effort aiming to provide an excellent mathematical code with applications in several areas such as building physics, pharmacy and agriculture - which was accomplished thanks to the assistance from my supervisors, the support from my friends and, mainly my mother who tirelessly helped me to move this work forward. This study was financed in part by the Coordenação de Aperfeiçoamento de Pessoal de Nível Superior - Brasil (CAPES) - Finance Code 001

List of Figures

1 Radiative intensity sketch in a direction $\hat{s}$. 6
2 HG function. 7
3 Radiative intensity at the boundaries. 9
4 Predicted moisture 10
5 Light weight wall. 11
6 Gradient pressure changes. 11
7 Temperature distribution. 13
8 Moisture distribution. 13
9 Moisture with high humidity 14
10 Multilayer - moisture after 12 hours of simulation. 14
11 Attic sketch. 15
12 Experimental temperature boundary conditions 17
13 Experimental boundary conditions - relative humidities values 17
14 Predicted heat fluxes at the roof inner surface. 18
15 Predicted heat flux portion. 18
16 Moisture content evolution. 19
17 Predicted moisture with CFD 26
18 Predicted temperature profile within the wall. 27
19 Predicted moisture within the wall and air velocity. 28
20 Predicted convective mass transfer coefficient at the surface "S1". 28
21 Predicted convective heat transfer coefficient at the surface "S1". 28
22 Predicted convective mass transfer coefficient at the surface "S2". 29
23 Predicted convective heat transfer coefficient at the surface "S2". 29
24 Predicted convective mass transfer coefficient at the surface "S3". 29
25 Predicted convective heat transfer coefficient at the surface "S3". 29
26 Museum room mesh 29
27 Statue and walls mesh details. 29
28 Temperature distributions within different physical domains 30
29 Moisture content distribution within the wall and the plaster statue. 30
30 Brick: two-dimensional approach - unit in mm. 32
31 Predicted temperature. 32
32 Predicted relative humidity. 32
33 Predicted moisture content. 33
34 Predicted temperature within the multilayered wall. 33
35 Experimental apparatus for MBV index assessment. 38
36 MBV index rating ref.[9]. 39
37 Plywood mesh 40
38 Plywood mesh details on interface. 40
39 Representation of plywood box in 2D. 41
40 Plywood moisture storage functions presented in the literature. 42
41 Plywood moisture storage functions presented in the literature. 43
42 Plywood mass evolution. 44
43 Relative humidity for plywood and air. 46
44 Water vapor mass fraction present in the air. 46
45 Relative Humidity distribution within the plywood box. 47
46 Mass flow along the left wall. 47
47 Mass flow along the right wall. 47

48 Mass flow along the bottom wall. 47
49 Mass flow along the top wall. 47
50 Sorption distribution. 48
51 Desorption distribution. 48

List of Tables

Table 1 Simulation data - homogeneous wall. 9
Table 2 Light weight wall - properties. 11
Table 3 Light weight wall - parameters. 12
Table 4 Multilayered wall - properties. 12
Table 5 Multilayered wall - parameters. 13
Table 6 Multilayered wall - Convective transfer coefficients. 13
Table 7 Radiative and thermal properties. 16
Table 8 Moisture and energy parameters for two different driving potentials. 23
Table 9 Simulation data - homogeneous wall. 25
Table 10 Hygrothermal properties - multilayered wall. 34
Table 11 Convective mass transfer coefficients - multilayered wall. 34
Table 12 Parameters. 35
Table 13 ANSYS-Fluent Macros used in the CFD-HAM model. 39
Table 14 Reference for wall symbols. 40
Table 15 MBV rating calculation for each simulation code. 48

Nomenclature

Subscripts

a	Air, ambient
b	Blackbody
$cond$	Conduction
$conv$	Convection
e	East boundary surface
eff	Effective
g	Gas
h	Heat
l	Water
lat	Latent
m	Mass
o	Dry material
p	Center volume
rad	Radiation
s	Spatial reference
sat	Saturated
suc	Capillary
sur	Surface
tot	Total
V	Elemental volume
v	Vapor
W	West boundary surface

Greek-letter notations

α	Thermal diffusivity $[m^2/s]$
β	Extinction coefficient $[1/m]$
$\boldsymbol{\xi}$	Gravity $[m/s^2]$
χ	Interpolation factor $[-]$
δ	Permeability $[s]$
ι	Characteristic lenght $[m]$
κ	Absorption coefficient $[1/m]$
λ	Hidraulic conductivity $[s]$
μ	Dynamic viscosity $[Pas]$
Ω	Solid angle $[sr]$
ω	Water content $[kg/m^3]$
Φ	Scattering phase function $[-]$
ϕ	Relative Humidity $[-]$
ψ	Weight Function $[-]$
ρ	Specific mass $[kg/m^3]$
σ	Scattering coefficient $[-]$
τ	Optical thickness $[-]$
υ	Convective transfer coefficient $[W/(m^2K)]$
ϖ	Scattering albedo coefficient $[-]$
ϱ	Reflectivity of media $[-]$
ϑ	Surface coefficient of water vapor transfer $[s/m]$
ζ	Direction cosine $[-]$

Mathematical symbols

∇	Nabla operator
∂	Operator for partial diferential
d	Operator for diferential

Roman-letter notations

$\boldsymbol{g}$	Flow $[kg/(m^2\ s)]$
$\boldsymbol{q}$	Heat $[W/m^2]$
$\boldsymbol{u}$	Density of air flow rate $[m/s]$
$\hat{s}$	Ordinate direction vector $[-]$
c	Specific heat capacity $[J/(kg\ K)]$
D	Mass diffusivity $[m^2/s]$
G	Grashof number $[-]$
g_r	Anysotropic grade $[-]$
H	Enthalpy $[J/kg]$
I	Radiative intensity $[W/(m^2sr)]$
k	Thermal Conductivity $[W/(m\ K)]$
L	Latent heat $[J/kg]$
M	Molar weight $[kg/mol]$

N	Nusselt number $[-]$	R_{ay}	Rayleigh number $[-]$
n	Index media $[-]$	R_e	Reynolds number $[-]$
P	Pressure $[N/m^2]$	T	Temperature $[K]$
P_r	Prandtl number $[-]$	t	Time $[s]$
R	Universal gas constant $[J/(mol\ K)]$	X	Effective resistance factor $[-]$
		y	Molar fraction $[-]$

Contents

Abstract i

Acknowledgments ii

List of Figures iv

List of Table v

Nomenclature vi

1 General Introduction 1

2 A model for predicting heat, air and moisture transfer through fibrous materials 3
2.1 Introduction . . . 3
2.2 Mathematical model . . . 4
2.2.1 Assumptions . . . 4
2.2.2 Moisture . . . 4
2.2.3 Energy . . . 5
2.2.4 Radiative Transfer Equation (RTE) . . . 6
2.2.5 Boundary conditions . . . 8
2.3 Model verification . . . 9
2.3.1 Homogeneous wall . . . 9
2.3.2 Light weight wall . . . 10
2.3.3 High humidity . . . 11
2.4 Case study . . . 14
2.5 Results . . . 16
2.6 Final remarks . . . 19
2.7 Acknowledments . . . 20

3 Advanced building hygrothermal modeling 21
3.1 Introduction . . . 21
3.2 Mathematical model . . . 22
3.2.1 Conservation equations . . . 22
3.2.2 Boundary conditions . . . 23
3.3 Methodology . . . 24
3.4 Model verification . . . 25
3.5 Results . . . 26
3.6 Final remarks . . . 35
3.7 Acknowledgments . . . 36

4 Assessment of Advanced Hygrothermal Modeling 37
4.1 Introduction . . . 37
4.2 Experimental Set-up . . . 38
4.3 Numerical . . . 39
4.4 Uncertainties . . . 41
4.5 Material Properties . . . 42
4.6 Simulation Procedure . . . 43
4.7 Results . . . 44
4.7.1 MBV index . . . 48

4.8 Final remarks 49
4.9 Acknowledgments 49

5 General Conclusions **50**

References **57**

1 General Introduction

The scarcity of natural resources drives the planet into a predictable and discouraging future, making it essential to limit or reduce energy consumption by opting for sustainable development. The amount of energy consumed in residential, commercial and industrial buildings tends to increase with the growth of the world population, considering the current energy demand. The world's energy consumption is expected to increased 28% until 2040 [1]. In Europe, 40% of total energy is used in buildings [2], which has determined the development of new technologies. Making a breakdown by category, the energy consumption in the residential sector exceeds the industrial one (https://www.eia.gov/consumption/). With this rate of energy growth, it is crucial to develop a strategy to improve the energy performance of residential and non-residential buildings. Building energy efficiency regulations - which set minimum standards for the building performance - aim at considerably reducing building energy consumption.

In this way, hygrothermal simulation tools may significantly contribute to sustainability in the construction sector so that the knowledge of heat and moisture transport mechanisms applied in buildings resulted in several mathematical models and tools published in the literature [3–6], contributing to build optimized workplaces focusing in energy saving and indoor air quality as well.

The challenge on modeling is to represent with accuracy the temperature and moisture content distributions within building porous envelopes and elements, to improve occupants health and to reduce energy consumption/demand and material deterioration risk [7]. In late eighties and in the nineties, one-dimensional heat and moisture codes through porous building elements were developed such as DELPHIN [8], MATCH [9], MOIST [10], WUFI [11] and UMIDUS [12, 13], based on different assumptions and driving potentials. The reader may refer to [14] for more details on some developed models. In the 2000's, some energy simulation codes such as Domus [15], BSim [16], WufiPlus [17], ESP-r [18] and EnergyPlus [19] have integrated moisture adsorption/desorption in their wall conduction models.

However, all those codes are considerably limited due to geometric complexities and to the boundary conditions (BC) related to the surrounding airflow. In addition, it is well known that the weather may play a significant role as BC such as the driving load rain [20] and solar radiation [21]. Those phenomena have been well studied, but the current simulation tools apply them in a simplified approach. For instance, within the wall, even containing a fibrous material, the thermal radiation is not propagated considering moisture migration. If so, it is done in a simplified way, considering a one-dimensional case. Another critical issue is how the current models calculate the heat and mass transfer convective coefficients. Most of codes use them with a flat value for the entire surface, or with local value to a customized case, however the well-known fluid mechanics dimensionless numbers such as Reynolds, Schmidt, and Sherwood are not used for calculating them.

Therefore, this work presents a new mathematical model to overcome the given gaps, which is fully coupled to a CFD software (ANSYS-Fluent) [22], providing a powerful hygrothermal tool to solve problems under complex geometries in one-, two- or three-dimensions. The original algorithm was first written in C - as a stand-alone code - for 1D cases (called CAR-HAM – Convective, Advective, and Radiative Heat, Air and Moisture) and, with some algebraic handling operations to use specific macros of the CFD code with some improvements, so that to create a second simulation code called (CFD-HAM) to solve complex multidimensional CFD-integrated cases concerning heat and moisture transfer.

The thesis is organized as follows. In Chapter 2, the one-dimensional heat, air and moisture (HAM) mathematical model, considering radiation in fibrous materials is presented. The boundary conditions are described in terms of diffusive and convective heat and moisture transport

as well as phase change. The simulation code is tested in three steps. First, the drying of an one-dimensional bar under isothermal conditions is simulated to verify the diffusion terms of the proposed model. Then, a thick layer under airflow presence is considered to verify the convective terms and, in the third step, to verify the thermal radiation of the new model – CAR-HAM, a residential attic insulation is simulated considering a fibrous material under moisture adsorption and desorption mechanisms.

Chapter 3 presents the coupling between the proposed model in Chapter 2 and the package ANSYS-Fluent by means of user-defined functions (UDF), providing calculations of the local convective heat and mass transfer formulas through complex surfaces. Different case studies are shown to illustrate the potentialities of the new tool. For instance, a conditioned museum room with a plaster statue represented by a complex profile is simulated. Additionally, 1D and 2D models, including the well known WUFI [11] software, have been used to simulate the temperature, relative humidity, and moisture distribution within a hollowed porous brick, which is widely used in the construction sector, but commonly simulated in a very simplified way. A multilayer wall composed of plaster and hollowed brick was considered, including buoyancy effects (for 2D simulations only).

In Chapter 4, an experimental set-up according to a Nordtest protocol is simulated to experimentally validate the proposed model. Indeed, the material is exposed in a moisture environment with cycles of relative humidity to calculate a moisture buffer value called MBV index that represents the hygroscopic buffering capacity of a porous building material. With a more sophisticated approach, take into account the airflow coupling, the proposed model verifies several cases published in the literature [20, 23, 24] to validate its application in cases involving heat and mass transfer processes through porous materials.

The three main chapters provide valuable information on creating a more sophisticated model to deal more accurately with the problem of moisture in buildings.

In Chapter 5, conclusions are addressed as well as some proposals for further work.

2 A model for predicting heat, air and moisture transfer through fibrous materials

Abstract. *A precise hygrothermal model is essential to predict the energy performance of building envelopes providing coupled transport of mass (moisture and air) and heat through porous elements, considering phase change and all heat transfer modes, including the radiative transfer through fibrous materials. Therefore, a new mathematical model, called CAR-HAM (Conductive, Advective, and Radiative Heat, Air and Moisture), is proposed to include the radiative transfer equation to calculate the thermal radiation effects within the porous materials to be taken into account in the energy balance. The moisture and the energy conservation equations are simultaneously solved using a fully implicit scheme and the MTDMA algorithm. The comparison of the proposed model considering some case studies such as attic insulation, bar drying, convection and high humidity (rain load) - showed a good agreement with experimental data available in the literature.*
Keywords: *Participating porous media, radiative heat transfer equation, moisture, hygrothermal performance of insulation materials.*

2.1 Introduction

Attenuation of heat and moisture transfer through roofs, specially in dwellings, is an efficient strategy to reduce energy consumption [25, 26]. Besides its effects on the energy balance, moisture can deteriorate insulation layers and cause mold growth [27].

Moisture transfer research has been presented since the beginning of the last century, for unsaturated porous media based on Darcy and Fick's laws as published in [3,4,6,28]. In building physics, the unsteady moisture transfer behavior research started with a simple case of a flat concrete roof [5]. Two models that were used as a reference for recent models were published in the 50's and in the 60's [4,28]. In the 80's some studies have shown the results of a synthesis over several works involving moisture laboratory measurements for conducting research on moisture behavior through fibrous insulations [29]. Over time, experimental data for a wide range of materials were collected and some properties were aproximated (e.g., permeability) to provide solutions for current mathematical models [30].

The heat and moisture coupling transfer in building physics started to be a topic of more intensive research in the early nineties and has originated many international projects such as IEA Annexes 14, 24, 41, 55 and the HAMSTAD European project [20,23]. A detailed review of mathematical models, numerical methods and simulation codes may be referred in [14]. Although all the international research efforts, no model in the field of building energy simulation has included the radiative heat transfer in the energy conservation equation, except as a boundary condition.

The radiation can be described by several numerical methods such as the zone method, Monte Carlo method, discrete transfer method and *PN* method, among others [31]. An attractive simplified method, so-called Discrete Ordinate Method (DOM) was developed in the 50's [21], and later, it was intensively studied by several authors [32, 33]. The radiation effect in fibrous media started with a simple mathematical model, isotropic scattering medium, and steady-state conditions [34]. Shortly later, it was considered anisotropic scattering medium, unsteady condition and the effect of fibrous media morphology with arbitrary optical thicknesses [35]. More sophisticated models were developed combining radiation and conduction applied to high porosity fiber thermal insulation materials under high temperatures [36, 37] where the thermal radiation plays a significant role. Some nanomaterials like aerogels [38], that significantly reduce

conduction/convection heat transfer, can have the radiative heat transfer improved in ambience temperature. Aiming to providing accuracy at reasonable calculation time, the radiative transfer equation (RTE) solution methods have been diversified with some techniques of angular and space discretization in a two-dimensional uniform Cartesian mesh. More focused in the field of building physics, some applied research regarding radiation in residential attics has been presented [39–41] denoting the importance of the radiative heat flux through insulation materials, which, in some cases, is even greater than the conductive heat transfer [39]. When the heat transfer process comprises the radiation, the traditional method for calculation is firstly solving the RTE, and then with the radiation flux, the energy equation is solved, but sometimes, the process is not so fast. So, later a new coupled numerical procedure for solving conductive and radiative heat transfer problems was introduced by Mazumder [42].

A lot of well-thought mathematical models are presented, and some of them include both radiative and heat transfer modes; however, no one includes moisture transport when both modes are considered, which may be relevant for some applications in the building physics field.

Therefore, to contribute to the progress of heat and mass transfer modeling in building physics, this paper presents and validates a mathematical model that considers radiation as an additional heat transfer mode so that insulation materials can be appropriately simulated as participating media to the phenomenon of scattering radiation under the presence of moisture.

The new combined heat and moisture transfer model denominated CAR-HAM (Conductive Advective and Radiative Heat, Air and Moisture), through insulation materials, should enable an accurate design of high-performance building envelopes and moisture safe constructions. The formulation is based on the model presented in the HAMSTAD project, adding the contribution related to radiation. The discretized equations are solved using the MTDMA algorithm [43, 44] to provide a coupled and stable solution of both energy and mass balances equations at the same iteration level. The Discrete Ordinate Method application provides the radiative heat transfer contribution.

In Section 2.2, the new mathematical model is presented; Section 2.3 provides its verification against data from literature, while Section 2.4 presents a case study and Section 2.5 some simulation results in an attic. In Section 2.6, the final remarks are addressed.

2.2 Mathematical model

2.2.1 Assumptions

Based on the mass and energy conservation equations, the CAR-HAM model takes into account the moisture and energy balance including the radiation contribution. The simulation code is based on the following assumptions:

- Temperature between $0^{o}\mathrm{C}$ and 80 $^{o}\mathrm{C}$;
- No hysteresis effects are presented;
- No chemical reactions are considered;
- Radiative properties do not change with moisture;
- Driving rain is taking into account as a Dirichilet boundary condition.

2.2.2 Moisture

Besides the model assumptions, vapor is considered as a perfect gas so that:

$$P_v = \rho_v \frac{RT}{M_l}\,, \tag{1}$$

where R is the universal gas constant, ρ_v, the density vapor, T, the temperature and M_l the molar weight of water. If liquid phase within the pore system is also taking into account, the two phases of water are assumed to be in equilibrium, satisfying Kelvin's equation so that the liquid pressure can be described as follows:

$$P_l = \rho_l \frac{RT}{M_l}\, ln\left(\frac{P_v}{P_{sat}}\right). \tag{2}$$

The P_v and P_{sat} mean vapor pressure and saturation vapor pressure, and ρ_l, the density of water. Then the suction pressure (P_{suc}) can be written as:

$$P_{suc} = P_g - P_l. \tag{3}$$

The moisture transfer through the porous structure can be divided into vapor and liquid flows by two transport phenomena: diffusion and advection [45]. Therefore, the moisture flow can be described by:

$$\boldsymbol{g}_{tot} = \boldsymbol{g}_v + \boldsymbol{g}_l\,. \tag{4}$$

In Eq. (4), $\boldsymbol{g_v}$ represents the vapor flow, while the other one, $\boldsymbol{g_l}$, refers to the liquid flow. The vapor flow can be expressed by diffusive and advective terms as:

$$\boldsymbol{g}_v = -\delta_v\, \boldsymbol{\nabla} P_v \;+\; \boldsymbol{u}\, \rho_v\,, \tag{5}$$

while the liquid flow is given by a sum of a diffusive term and a term due to the gravitational forces:

$$\boldsymbol{g}_l = -\lambda\, \left(\boldsymbol{\nabla} P_{suc} - \rho_l \boldsymbol{\xi}\right)\,. \tag{6}$$

In Eq. (5), ν_v refers to the moisture dependent vapor permeability, and $\boldsymbol{u}$, the density of air flow rate. In Eq. (6), λ means liquid water permeability and, ξ, the gravity. So, in the vectorial form, the mass balance equation for a porous media can be written as,

$$\frac{\partial \omega}{\partial t} = -\boldsymbol{\nabla} \cdot \boldsymbol{g}_{tot}\,, \tag{7}$$

were ω refers to the water content.

2.2.3 Energy

The three heat transfer modes are considered in the unsteady energy balance equation written as:

$$\frac{\partial H}{\partial t} = -\boldsymbol{\nabla} \cdot \left(\boldsymbol{q}_{tot}\right), \tag{8}$$

and the enthalpy can be defined as:

$$H = \rho_o c T, \tag{9}$$

where the specific heat **c** of the porous material is defined by:

$$c = c_o + \frac{\omega\, c_l}{\rho_o}. \tag{10}$$

In Eq. (10), c_o is the dry-basis specific heat, c_l, the liquid water specific heat, ω the moisture content and, ρ_o, the dry-basis specific mass.

Eq. (8) represents the enthalpy variation in time, which is equal to the divergent of total heat transfer (q_{tot}) that can be represented by:

$$\boldsymbol{q}_{tot} = \boldsymbol{q}_{cond} + \boldsymbol{q}_{conv} + \boldsymbol{q}_{rad} + \boldsymbol{q}_{lat}, \tag{11}$$

where $\boldsymbol{q}_{cond}$, $\boldsymbol{q}_{conv}$ and $\boldsymbol{q}_{lat}$ can be written as:

$$\begin{aligned} \boldsymbol{q}_{cond} &= -k\nabla T; \\ \boldsymbol{q}_{conv} &= \boldsymbol{u}\rho_a c_a T; \\ \boldsymbol{q}_{lat} &= \boldsymbol{g}_v L_v + \boldsymbol{g}_l c_l T. \end{aligned}$$

In Eq. (11) right-hand side, the first term represents the diffusive heat transfer and the second one is associated to the heat flux by air convection; the next two terms represent the latent heat contributions by moisture flow - latent and sensible - and, finally, the last one ($\boldsymbol{q}_{rad}$) is related to the radiative heat transfer mode that needs to be calculated previously by RTE (Radiative Transfer Equation); k is the thermal conductivity of the medium, ρ_a, the air density, c_a represents the specific heat capacity at constant pressure and L_v is the latent heat of evaporation.

2.2.4 Radiative Transfer Equation (RTE)

The RTE is an integro-differential equation whose solution requires special treatment to be numerically solved by methods such as DOM (Discrete Ordinate Method).

Considering a medium with contributions of emission, absorption and scattering of any given direction $\hat{s}$ (see Fig. 1) [46]:

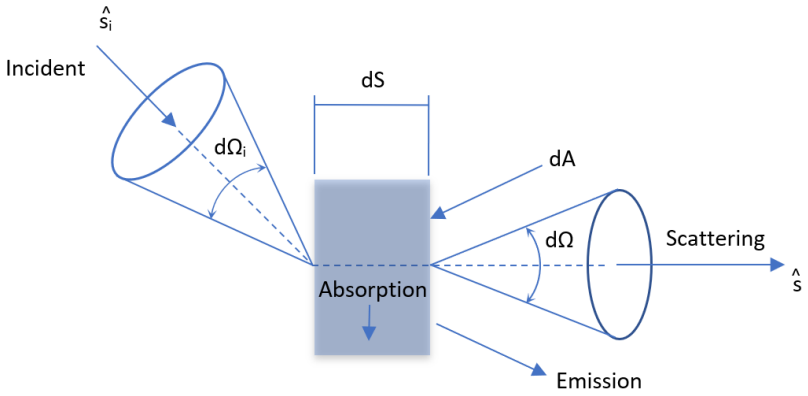

Figure 1: Radiative intensity sketch in a direction $\hat{s}$.

$$\hat{s}\cdot\nabla I = \kappa I_b - \beta I + \frac{\sigma}{4\pi}\int_{4\pi} I(\hat{s}_i)\Phi(\hat{s},\hat{s}_i)d\Omega_i\,, \tag{12}$$

where Φ is the phase function that describes the changes of direction of a given ray from one direction $\hat{s}$ to another direction $\hat{s}_i$. In the right-hand side, the first term represents the local intensity emitted; the second one, the intensity absorbed in the medium. The variables κ and β are the absorption and extinction coefficients, respectively. Henyey-Greenstein phase function describes the anisotropic scattering:

$$p(\zeta) = \frac{1}{2}\frac{1-g_r^2}{[1+g_r^2-2g_r\zeta]^{3/2}}\,, \tag{13}$$

where ζ is the direction cosine represented by $\zeta = \cos(\theta)$ and g_r stands for the anisotropic grade. For g_r >0, foward scattering is dominant; otherwise, backscattering predominates (see Fig. 2). It was assumed an anisotropic grade of $g_r = 0.9$ (typical value for glass wool).

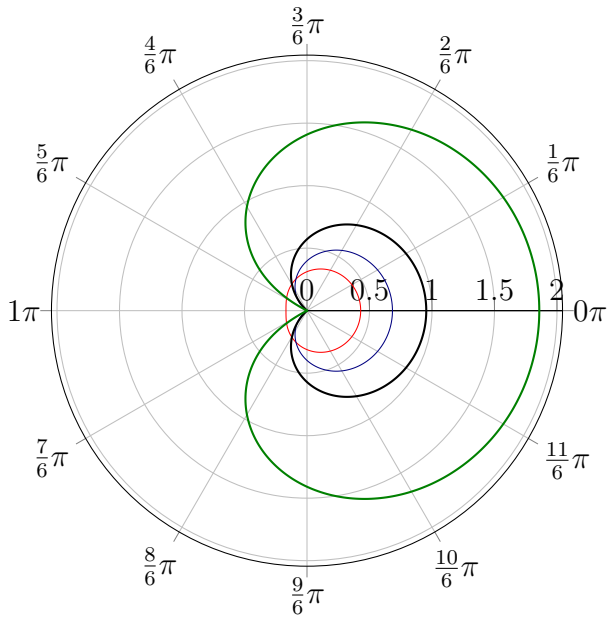

Figure 2: Henyey Greenstein function; gr=0.1, red; gr=0.3, blue; gr=0.5, black; gr=0.9, green. Radi axis is plotted on logarithmic mode.

Integrating Eq. (12) over all solid angles, we obtain [46]:

$$\nabla \cdot \boldsymbol{q}_{rad} = \kappa(4\pi I_b - \int_{4\pi} I d\Omega). \tag{14}$$

Eq. (14) describes the radiative energy from a control volume that is regarded in energy equation as a source term. Applying the Discrete Ordinate Method (DOM), it can be rewritten as

$$\nabla \cdot \boldsymbol{q}_{rad} = \kappa(4\pi I_b - \sum_{j=1}^{n} I_j \psi_j) \, . \tag{15}$$

The weights ψ_j associated to the direction $\hat{s}_i$ represent the numerical quadratures which replace the integral. A previous calculation of intensity solves Eq. (15). So applying the discrete ordinates method, introducing the optical coordinate τ and the scattering albedo ϖ, Eq. (12) becomes:

$$\zeta_i \frac{dI_i}{d\tau} = (1 - \varpi) I_b - I_i + \frac{\varpi}{4\pi} \sum_{j=1}^{n} I_j \psi_j, \tag{16}$$

or in a short form:

$$\zeta_i \frac{dI_i}{d\tau} + I_i = Sp_i, \tag{17}$$

with

$$Sp_i = (1 - \varpi) I_b + \frac{\varpi}{4\pi} \sum_{j=1}^{n} I_j w_j, \tag{18}$$

where Sp_i represents the source term. Applying Eq. (18) for each control volume of any given discretized form, it is possible to calculate the intensities of the considered domain with a previous temperature field.

The RTE equation is solved by the field intensity that depends on the temperature field. By means of the discrete ordinate method, it is possible to solve Eq. (17) with some angular and spatial discretizations. So, applying the integral over an elemental volume:

$$\int_V \left(\zeta \frac{\partial I}{\partial s} = -\beta I_p + \beta S_p \right) dV \, , \tag{19}$$

where **V** is the volume and **s** refers to the spatial reference. The S_p was defined according to the Eq. (18). For an one-dimensional case, the volume is Δx, and after some arrangements, it yields:

$$\zeta \left(I_e - I_w \right) = (-I_p + S_p) \beta \Delta x \, . \tag{20}$$

The subscripts **e** and **l** refer to the east and west boundary faces of the control volume. Isolating I_e, one has:

$$I_e = -\frac{\beta \Delta x}{\zeta} I_p + \frac{\beta \Delta x}{\zeta} S_p \, . \tag{21}$$

To each element of volume is applied the scheme described by "weighted diamond differencing" [32] yields:

$$I_p = I_e \chi + (1 - \chi) I_w \, . \tag{22}$$

The χ means the interpolation factor. Combining Eq. (22) with Eq. (21) obtain:

$$I_e = \frac{I_w \left(\gamma - \alpha \right) + \alpha S_p}{\gamma} \, , \tag{23}$$

with $\gamma = (1 + \alpha)$. Operating similarly, the intensity over the volume center I_p can be found isolating I_e in Eq. (22) and replacing it in Eq. (21).

With the temperature field, the intensities over the domain can be calculated. Therefore, initial temperatures are first given to get the intensities, then the divergent of thermal radiation is calculated by Eq. (15) and accounted for the energy in Eq. (8). The process is repeated until it reaches the convergence.

2.2.5 Boundary conditions

The diffusion and convection fluxes have been considered in the boundary condition (BC) for the moisture flow into/out the structure. The moisture BC can be written as:

$$\boldsymbol{g}_v = \pm \vartheta \nabla P + \boldsymbol{u} \rho_v \, . \tag{24}$$

In Eq. (24), $\boldsymbol{g}_v$ is the moisture flow and ϑ is the convective mass transfer coefficient. Similarly, the energy boundary condition can be written as:

$$\boldsymbol{q} = \pm \upsilon_h \nabla T + \boldsymbol{u} \rho_a c_a T_a + \boldsymbol{g}_l c_l T_a + \boldsymbol{g}_v L_v \, , \tag{25}$$

where, υ_h is the convective heat transfer coefficient.

The boundary conditions for radiative intensities can be written as:

$$\tau = 0, \;\; I_{(0,\zeta)} = \varrho_w I_{(0,-\zeta)} + \left(1 - \varrho_w \right) n^2 I_b \left(T_w \right) \rightarrow \zeta > 0 \, , \tag{26}$$

$$\tau = \tau_o, \;\; I_{(\tau_o,\zeta)} = \varrho_e I_{(0,\zeta)} + \left(1 - \varrho_e \right) n^2 I_b \left(T_e \right) \rightarrow \zeta < 0 \, , \tag{27}$$

where ϱ is the reflectivity and $\boldsymbol{n}$ is the medium index. The subscripts (*w*,*e*) refer to the **west** and **east** boundaries (see Fig. 3).

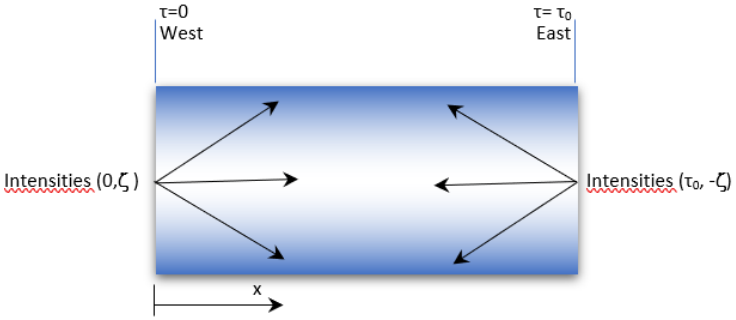

Figure 3: Radiative intensity at the boundaries.

2.3 Model verification

In this section, the CAR-HAM validation involves comparison with literature data where the performed cases include isothermal conditions, air convection, liquid migration and radiation. In the first step, a concrete bar exposed to low relative humidity surrounding air is analyzed, where its moisture content decreases with time (Homogeneous wall). Then, mass transport, by diffusion and advection, computes the relative humidity distribution within the wall (Lightweight wall). Besides, it is simulated a multilayer wall under step function boundary conditions with high humidity - higher than 99% and finally, the simulation code evaluates the heat, moisture, and radiative transport through a residential roof (Attic).

2.3.1 Homogeneous wall

In this first simulation, the moisture and heat transfer occurs through a homogeneous wall, with no air pressure difference, under isothermal conditions. The main data is described in Table 1.

Sorption isotherm (ω)	$116 \cdot (1 - ln\phi/0.118)^{0.869}$	kg/m^3
Vapour diffusion (δ_v)	$1.0 \cdot 10^{-15}$	s
Moisture diffusivity (D_l)	$6.0 \cdot 10^{-10}$	m^2/s
Thermal conductivity (k)	0.15	$W/(mK)$
Specific heat capacity (c_o)	800	$J/(kgK)$
Density (ρ_o)	525	kg/m^3
Thickness (e)	0.2	m
Latent heat (L_v)	56.8	J/kg
Convective mass transfer coeff. (ϑ)	$1.0 \cdot 10^{-3}$	s/m
Convective heat transfer coeff. (υ_h)	25	$W/(m^2K)$
Temperature (T) (internal and external)	293.15	K

Table 1: Simulation data - homogeneous wall.

Fig. 4 shows the predict moisture simulated by CAR-HAM and Others[1]. It is noticed that

[1]Others represent average values obtained by the following institutes and universities: KUL (University of Leuven), TECHNION (Technion Israel Institute of Technology), TUD (Technical University of Dresden), CTH (Chalmers University of Technology), NRC (National Research Council of Canada) and IBP (Fraunhofer Institute of Building Physics). More details can be found in [20]. PM stands for the present proposed model.

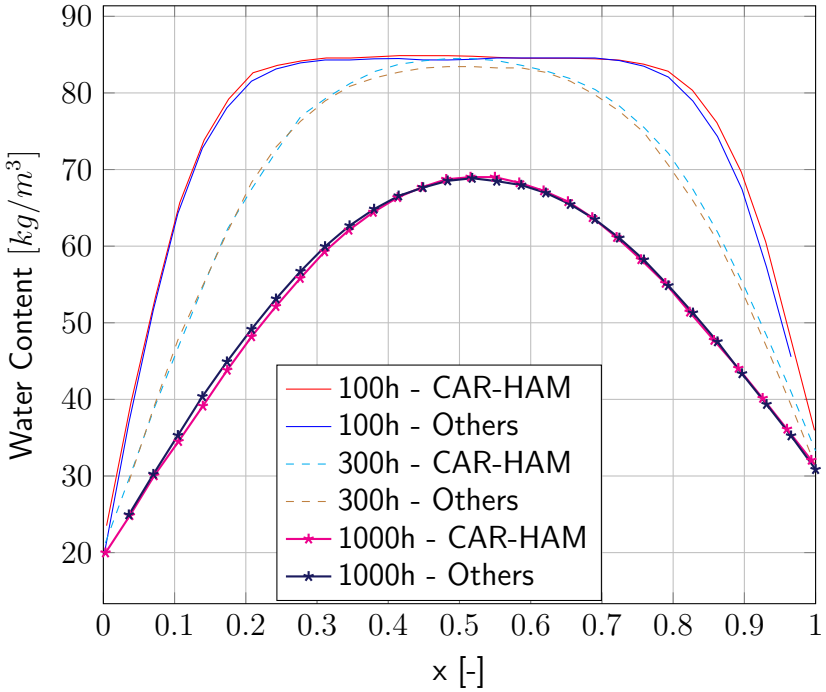

Figure 4: Homogeneous wall - predicted moisture.

the moisture movement occurs due to an important gradient of relative humidity between the material and the surrounding air. In this simulation, there is a sudden change in relative humidity, and the direct effect is noted at the two ends of the bar. Initially, the concrete slab was at a 95% relative humidity, and after 100 hours of simulation, the bar ends present a decrease higher than 60% of water moisture content, while the central region kept unaltered. After 300 hours of simulation, the diffusion moisture transport mode reaches the whole material, when there is a humidity decrease throughout the bar. At t=100 h, the distribution of water content across the wall has a significant difference with the boundaries, and this gradient effect increases the liquid and vapor diffusion moisture flow. The curves are not symmetric due to the difference between internal and external relative humidities. In this benchmark that involves only diffusion phenomena under isothermal conditions, the results had a perfect agreement with the original simulations [20]. All simulations have used a mesh with 30 points and a time step of 3600 s.

2.3.2 Light weight wall

A thick single layer is exposed to the airflow and to a large variation of temperature and humidity. Fig.5 shows schematically the wall and the boundary conditions. Tables 2 and 3 present the properties and parameters of the test case. In this simulation, the airflow is a function of external pressure gradient that changes with time, according to Fig.6. As initial conditions, the temperature of material is 20^0C and the relative humidity is 95%.

Until the twentieth day, the moisture content increases rapidly within the wall, due to a pressure gradient that promotes the transport of mass. At a time of 20 days, there is a moisture peak and the maximum concentration due to air infiltration is reached. The water content is concentrated at external face because the air flow from the indoor enters into the wall, carrying the moisture to the opposite surface. The internal surface coefficient of water (ϑ) vapor is higher than the external one, which promotes the high level of mass migration near the external surfaces, accumulating water content in this region. In the opposite way, the temperature suddenly drops (more than 20 ^0C). Besides, the moisture content yields a high effect on thermal conductivity, so

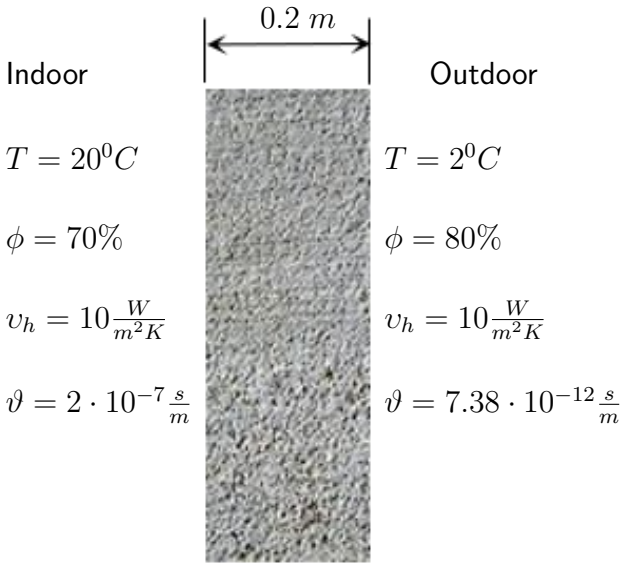

Figure 5: Light weight wall.

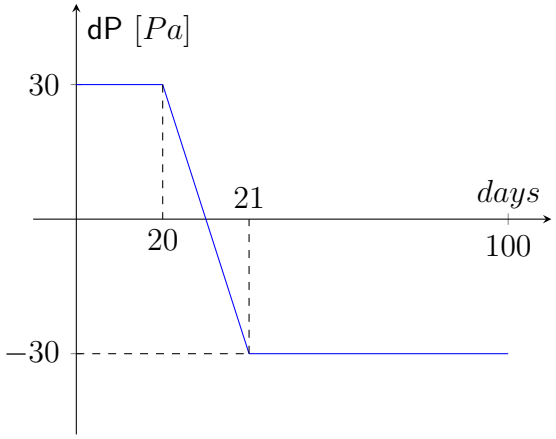

Figure 6: Gradient pressure changes.

Sorption isotherm (ω)	$\omega_s \sum_{i=1}^{N} k_i / \left(1 + (b_i P_{suc})^{n_i}\right)^{m_i}$	kg/m^3
Vapour diffusion (δ_v)	$(M_l/RT)D_v$	s
Hydraulic conductivity (λ)	$e^{\sum_{i=0}^{5} a_i(\omega/\rho_l)^i}$	s
Thermal conductivity (k)	$k_o + k(\omega/\rho_l)$	$W/(mK)$
Air flow rate ($\boldsymbol{u}$)	$C_v \nabla P$	m/s

Table 2: Light weight wall - Ref. [20].

the temperature at the interior of material changes rapidly. After 20 days, the pressure gradient decreases linearly (Fig.(6)) and the flow direction changes, resulting in a low humidity at the end of simulation as shown in Fig.(8). In Fig.(7), as an isothermal case, the capillary moisture transport process occurs independently of temperature gradients.

A non-uniform mesh was used in this simulation with 100 nodal points and a 80 s time step. With those parameters, the CAR-HAM transfer model provided a good agreement with the literature data.

2.3.3 High humidity

A two-layered wall is simulated for 5 days with moisture and heat exchanges between neighboring air and wall surfaces. The external surface is exposed to mixing boundary conditions, comprising rain load, heat and mass convection. The airflow is neglected. When rain occurs, the wall surface is saturated and the relative humidity almost reach the unity. The thicker part (with 200mm) of the wall is the external side and the finishing material is located at the internal part with 20mm of thickness. Initially, the wall interior is set to 20^0C of temperature and the water content to 0.4 kg/m^3 and 47.5 kg/m^3 at the external and internal surfaces, respectively. In Tables 4, 5 and 6 information about coefficients, parameters and properties of wall is provided.

Figure 9 shows a very well agreement of simulated codes of literature and the CAR-HAM model, illustrating several water content peaks at the surface that was submitted to high humidity values. Some differences can be seen in Fig. 9, especially at 20 hours of simulation: CAR-HAM presents greater storage of water content of almost 10%. The storage water variation during the time is very sensitive and depends on the choosen potential. After 80 hours of simulation,

Water Retention		
m_i	$1 - 1/n_i$	$-$
ω_{sat}	871	kg/m^3
$k1$	0.41	$-$
$k2$	0.59	$-$
$b1$	0.006	$1/m$
$b2$	0.012	$1/m$
$n1$	2.4883	$-$
$n2$	2.3898	$-$
Vapor Diffusion		
D_a	$26.1 \cdot 10^{-6}$	$-$
η	$1 - (\omega/\omega_{sat})$	$-$
D_v	$(D_a\eta)/(\mu_o(1-p)(\eta^2+p))$	m^2/s
μ_o	5.6	$-$
p	0.2	$-$
Liquid Water Diffusion		
$a0$	-46.245	$-$
$a1$	294.506	$-$
$a3$	3249	$-$
$a4$	-3370	$-$
$a5$	1305	$-$
Thermal Conduction		
k_o	0.06	$W/(mK)$
k	0.56	$W/(mK)$
Heat Capacity		
ρ_o	212	kg/m^3
c_o	1000	$J/(kgK)$
Convection		
C_v	$3.0 \cdot 10^{-5}$	$m/(sPa)$

Table 3: Light weight wall - Ref. [20].

External material		
Sorption isotherm (ω)	$157\left(\sum_{s=1}^{2} l_i\left(1+(c_iP_{suc})^{n_i}\right)^{m_i}\right)$	kg/m^3
Vapour diffusion (δ_v)	$(M_l/RT)D_v$	s
Hydraulic conductivity (λ)	Details in [23]	s
Thermal conductivity (k)	$0.5 + 0.0045\omega$	$W/(mK)$
Finishing material		
Sorption isotherm (ω)	$209\left(\sum_{s=1}^{2} l_i\left(1+(c_iP_{suc})^{n_i}\right)^{m_i}\right)$	kg/m^3
Vapour diffusion (δ_v)	$(M_l/RT)D_v$	s
Hydraulic conductivity (λ)	Details in [23]	s
Thermal conductivity (k)	$0.2 + 0.0045\omega$	$W/(mK)$

Table 4: Multilayered wall - Ref. [20].

variations of moisture can be noticed that may cause numerical errors, as the properties are strongly moisture dependent in the region with high water content. The moisture transportation goes through the layers due to hard external conditions such as condensation on the outer surface,

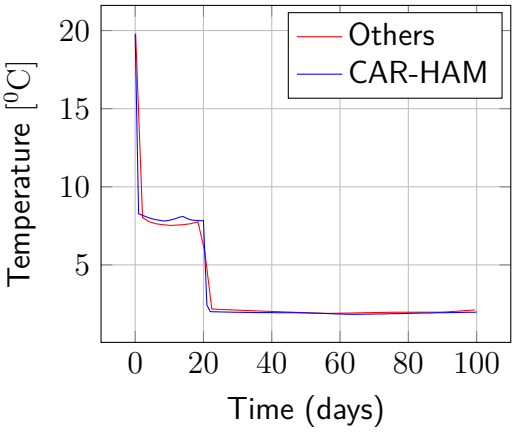

Figure 7: Light weight wall - predicted temperatures.

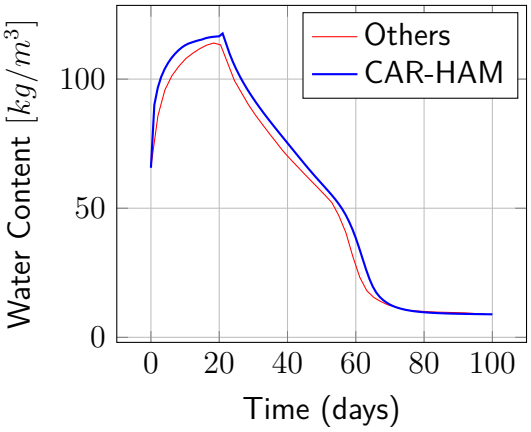

Figure 8: Light weight wall - predicted moisture.

External material		
m_i	$1 - 1/n_i$	–
n_1	1.65	–
n_2	6.0	–
l_1	0.3	–
l_2	0.7	–
c_1	$1.25 \cdot 10^{-5}$	–
c_2	$1.80 \cdot 10^{-5}$	–
D_a	$(26.1 \cdot 10^{-6})\,/30$	m^2/s
η	$1 - (\omega/157)$	kg/m^3
D_v	$(D_a\eta)/(0.503\eta^2 + 0.497)$	m^2/s
ρ_o	2005	kg/m^3
c_o	840	$J/(kgK)$
Finishing material		
m_i	$1 - 1/n_i$	–
n_1	1.27	–
l_1	1.0	–
c_1	$2.0 \cdot 10^{-6}$	–
D_a	$(26.1 \cdot 10^{-6})\,/3$	m^2/s
η	$1 - (\omega/209)$	kg/m^3
D_v	$(D_a\eta)/(0.503\eta^2 + 0.497)$	m^2/s
ρ_o	790	kg/m^3
c_o	870	$J/(kgK)$

Table 5: Multilayered wall - Ref. [20].

	Internal	**External**	
Convective heat transfer coeff.(υ_h)	25	8	$W/(m^2K)$
Convective mass transfer coeff.(ϑ)	$2.0 \cdot 10^{-7}$	$3.0 \cdot 10^{-8}$	s/m

Table 6: Multilayered wall - Convective transfer coefficients.

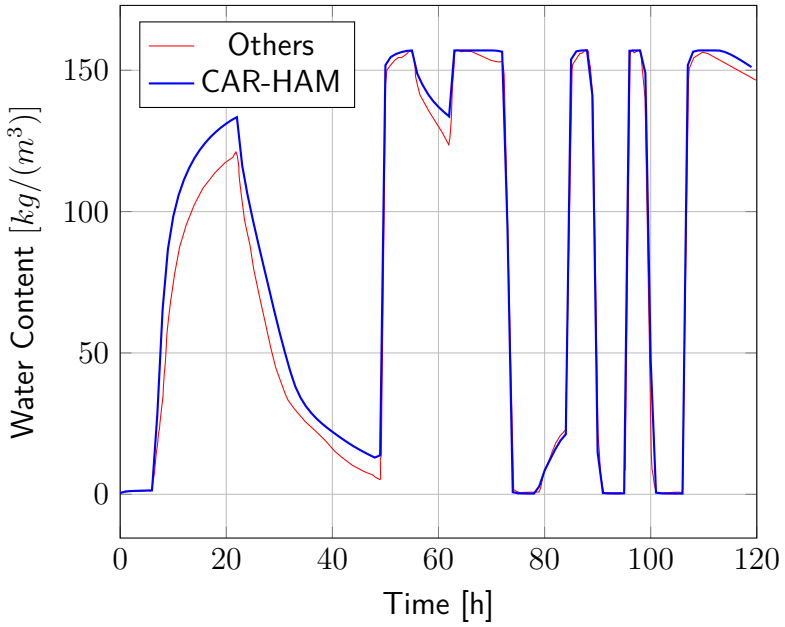

Figure 9: Wall under high humidity and external hard conditions.

high gradients of temperatures and the different liquid transfer rates for each material. In this case, the materials have very different hygroscopic behaviors that increase the discontinuity of moisture content value at the interface, as shown in Fig.10. Besides, the proposed model presents an additional of 10% of water content in the outer material due to its derivatives are sensitive and may produce some variations over total moisture distribution within the material.

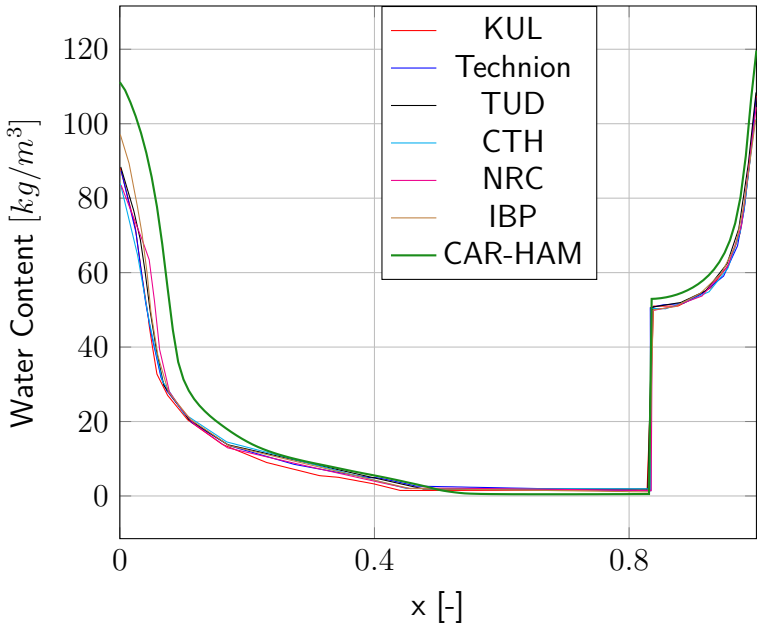

Figure 10: Multilayer - moisture after 12 hours of simulation.

2.4 Case study

In this case (Fig. 11), the aim is to study the substrate thickness variation (called "phenolic binder") within insulation material and its influence on water content migration. Radiation is

considered, for a gray and isotropic porous medium, and the boundary condition is of Dirichlet type; the temperature and the relative humidity values were taken from insulation boundaries and data was recorded every 15 minutes. For the simulation a non-uniform mesh with 33 points was considered, for a 300 s time step.

As shown in Fig.11, the fibrous medium is placed in contact with gypsum board until it reaches the surface ($y = y_0$). Specifically, at this surface, the boundary condition is of the third type where the temperatures were measured at a distance of 50 mm above of surface (attic air). The storage capacity of material $dw/d\phi$ was derived from a generic function of moisture content for a porous medium according to the equation of Brunauer-Emmet-Teller (BET). So, the typical fiberglass isotherm was approximated by:

$$W = \frac{W_m C \phi}{[1-\phi]\,[1+(C-1)\,\phi]}, \tag{28}$$

where W_m and C are empirical constants (their values are 0.01 and 50, respectively - used for adsorption; others values can be found in the literature for the sorption); ϕ refers to the relative humidity.

The effect of hysteresis was disregarded. In the original simulation, the insulating storage capacity accounting for the radiative effects was evaluated changing from 5% to 40% of the weight of a desiccant phenolic binder (PB). In the proposed model, the heat, moisture and thermal radiation transport is coupled, considering anisotropic medium.

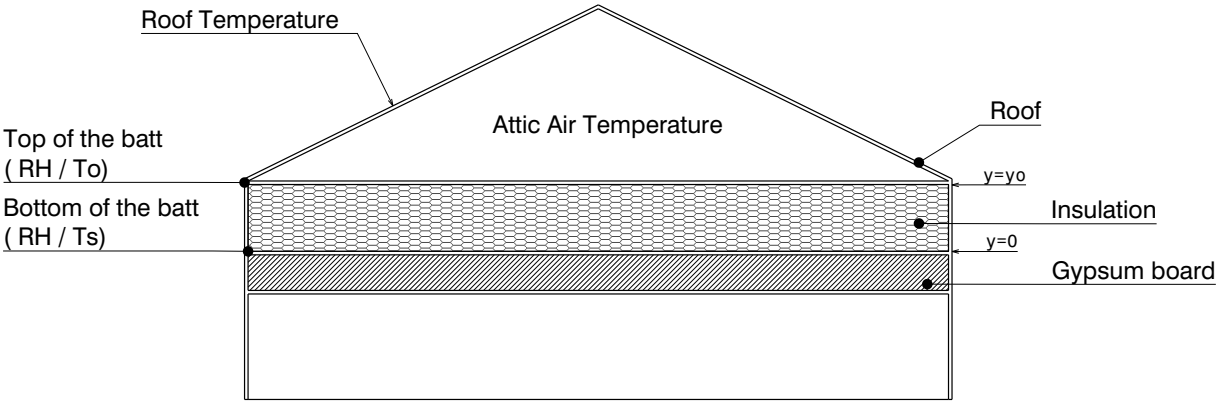

Figure 11: Attic sketch - Ref. [41].

The top of insulation receives radiation from roof. The experimental data measured is located on $y = 0$ and $y = y_0$ ordinates. The properties of fiberglass affects about 40% by weight of PB coating. Some assumptions and constraints for this simulation have been additionally considered:

- Dry - basis specific mass - even for PB - is unchangeable;
- Hysteresis phenomenon is neglected;
- Henyey-Greenstein function was adopted as phase function;
- Within the fibrous medium, the convection and the gravity effects were neglected.

The vapor and liquid flow values, from Table 7, are the final ones. They have to be converted to provide the potential adopted at the moisture and energy conservation equations (vapor pressure -P_v). On original data, the vapor flux is defined as follow:

Density (ρ)	12.0	kg/m^3
Heat capacity (c)	844.4	$J/(kgK)$
Thermal cond. (k)	$a + bT + 8.5537 \cdot 10^{-5}$	$W/(mK)$
	$a = 4.97576 \cdot 10^{-3}$	
	$b = 7.00025 \cdot 10^{-5}$	
Single scat. albedo (ϖ)	0.201	
Extinction coef.(β)	3.70	cm^{-1}
Vapor flux (δ_v)	$12 \cdot 10^{-5}$	m^2/s
Liquid flux (λ)	$1.19 \cdot 10^{-9}$	m^2/s

Table 7: Radiative and thermal properties - Ref. [41].

$$\boldsymbol{g}_v = \delta_v \nabla \rho_v. \tag{29}$$

Neglecting the convective term, the vapor diffusion is calculated by Eq. (5), and from the general gas law, can be written as:

$$\boldsymbol{g}_v = -\left[\delta_v \frac{M_l}{RT}\right] \nabla P_v. \tag{30}$$

For the proposed model, the vapor flux has unit s - according to Eq. (30), while at Eq. (29) is considered m^2/s as vapor flux unit. In this way, combining these equations, the properly value for the vapor flow can be used for the simulation case.

The same way is used to calculate the liquid flow ($\boldsymbol{g}_l$):

$$\boldsymbol{g}_l = \lambda \nabla \rho_l. \tag{31}$$

From Kelvin's law and combining it to Eq.6 - excluding gravitational forces, we obtain:

$$\boldsymbol{g}_l = -\left[\frac{\lambda M_l}{RT \ln\left(P_v/P_{sat}\right)}\right] \nabla P_{suc}. \tag{32}$$

With the same approach used for the vapor flow unit conversion, Eq. (31) and Eq. (32) , are combined to get the correct value for liquid flow to be used at the proposed model.

The boundary conditions have been assumed according to the original simulation [41] as shown in Figs.12 and 13 that represent the temperature and relative humidity values measured for a fiberglass insulation.

2.5 Results

After carrying out the the CAR-HAM model verification, simulation results are presented and also compared to a literature case related to residential attic insulation [41], for a summer period.

The following equation defined the total heat flux calculated through the insulation:

$$\boldsymbol{q}_{total} = -k\nabla T - \left(\delta_v \nabla P_v\right) L_v - \left(\lambda \nabla P_{suc}\right) c_l T + \boldsymbol{q}_{rad}\,, \tag{33}$$

where the terms from left to right on the right-hand side are: conductive heat flux, phase change heat flux, sensible liquid phase heat flux and radiation heat flux.

The results in Fig. 14 represent the total heat flux over simulation during one summer day due to high temperatures and high relative humidities. The original simulation adopted R-19 fiberglass insulation batt, with PB varying from 5% to 40%. The present simulation considered

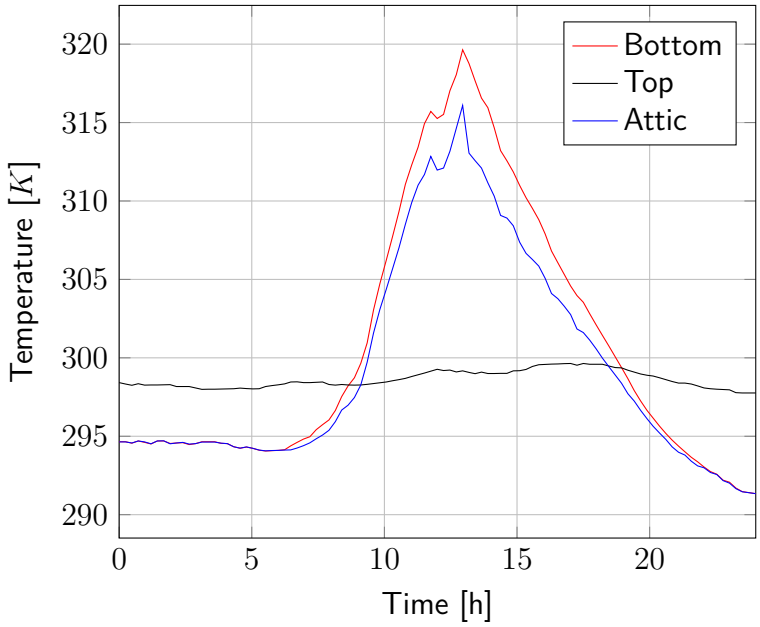

Figure 12: Experimental temperature boundary conditions - Ref. [41]

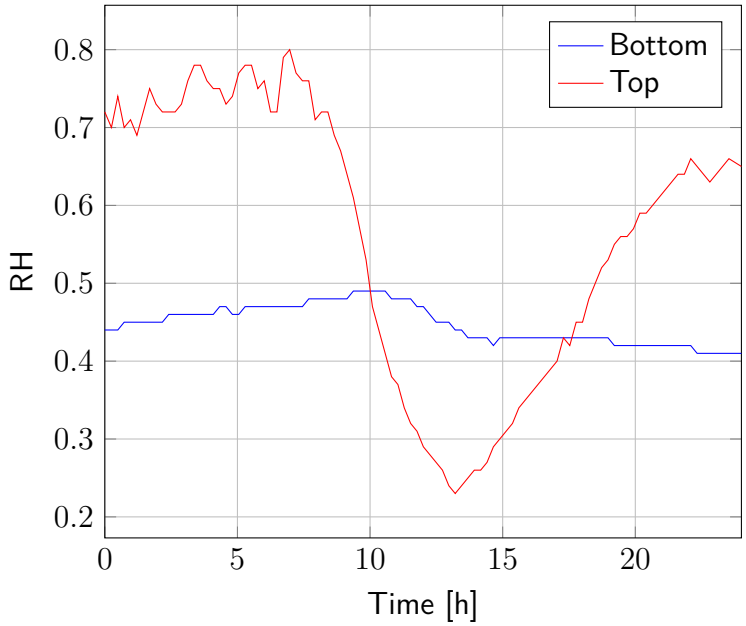

Figure 13: Experimental boundary conditions - relative humidities values - Ref. [41]

the insulation with 20% and 40% of desiccant. Fig.14 shows the CAR-HAM model considering two options: the first one simulates an isotropic medium, i.e., without anisotropic grade (CAR-HAM GR=0.0), and the second one, considers an anisotropic grade of 0.9 (CAR-HAM GR=0.9). Besides, it is shown the original data with PB changes and the simulation done by [39, 47]. This last simulation have neglected the moisture transport (only conduction and radiation). As shown in Fig. 14, the results of the five simulations are in good agreement, except the one that uses as anisotropic grade (expected solution since the original data was simulated in an isotropic medium). In this case, the radiative flux contributes for the total heat flux-that is noticeable at peak flux (13h) around 30%. Considering the original data, the insulation with 20% of desiccant allows a more significant heat flux than insulation with 40% that occurs due to increased hygroscopic with rising PB. The vapor pressure gradient increases (and mass diffusion

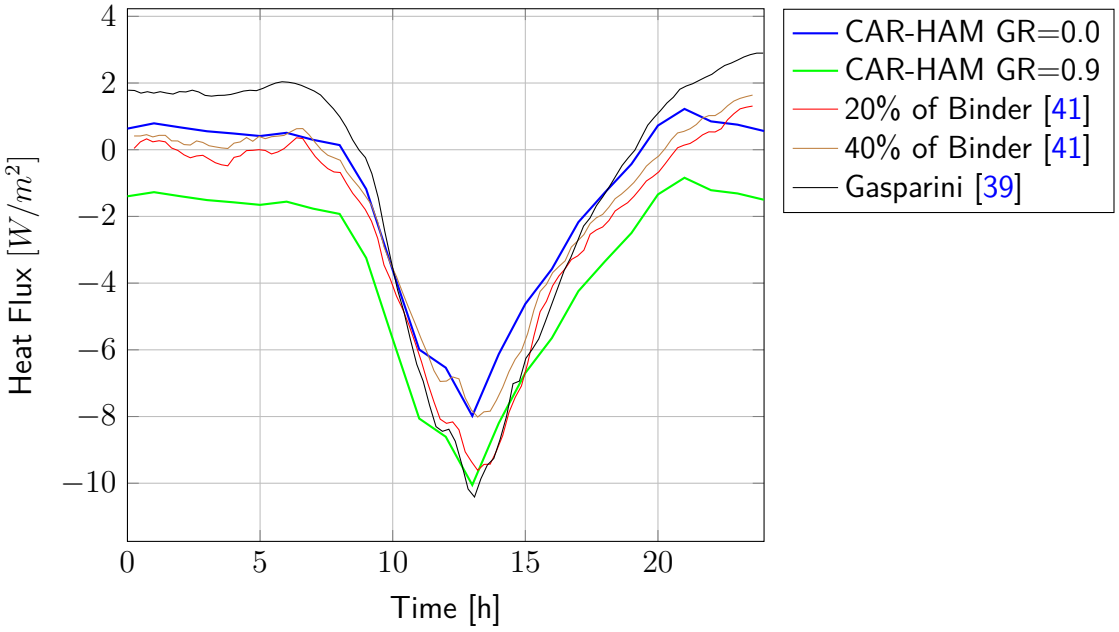

Figure 14: Predicted heat fluxes at the roof inner surface.

as well) with high desiccant concentration, while the latent heat (without temperature changes) becomes more relevant amend the overall heat transfer at the substrate, with the decrease shown in Fig.14. Changing to 20% of PB, there is a heat flux increase of $2W/m^2$.

Near 13 hours of simulation, there is a negative peak of heat flux. At this time, the roof temperatures reach a high value and the insulation is exposed to the most significant gradients of temperature and the negative signal means an incoming heat flux. There are some discordances between simulations before and after the heat peak flux. The one predicted by Gasparini [39] shows until 12h of simulation the highest heat flux within the substrate. In this case, both moisture storage function of fiberglass and its thickness were estimated and due to that, the model results presented slight differences from literature data. Additionally the third-type boundary

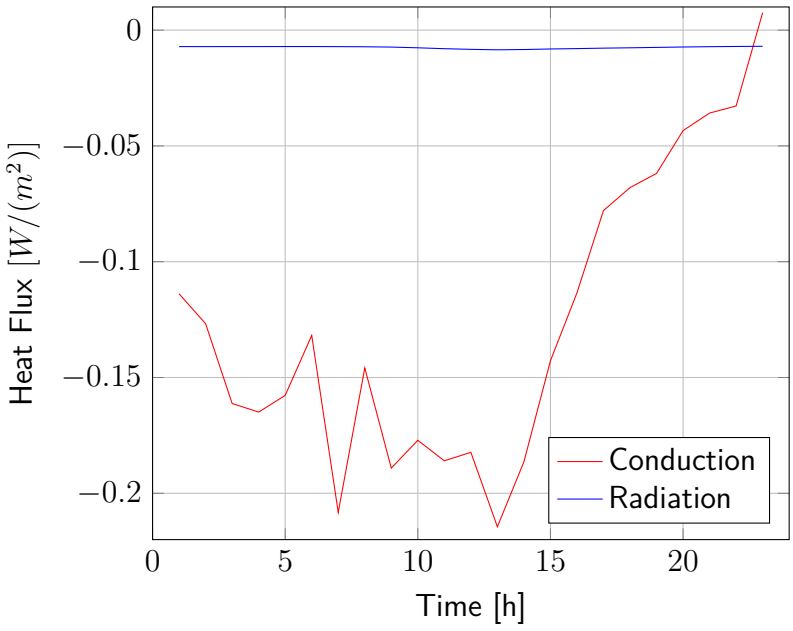

Figure 15: Predicted heat flux portion.

condition at $y = y_0$ presents quite a difference at the overall heat flux if changed it to a constant temperature.

Figure 15 shows the heat transfer modes distribution through the insulation. The greater heating portion is the conductive heat tranfer that represents almost the total heat flux. Throughout the residential attic insulation, the majority of energy transfer is related to phase change. The other ones, barely impact on the overall heat flux. The water content function [48] within the insulation is very small, as a result of adopting a generic fiberglass, according to Eq. (28).

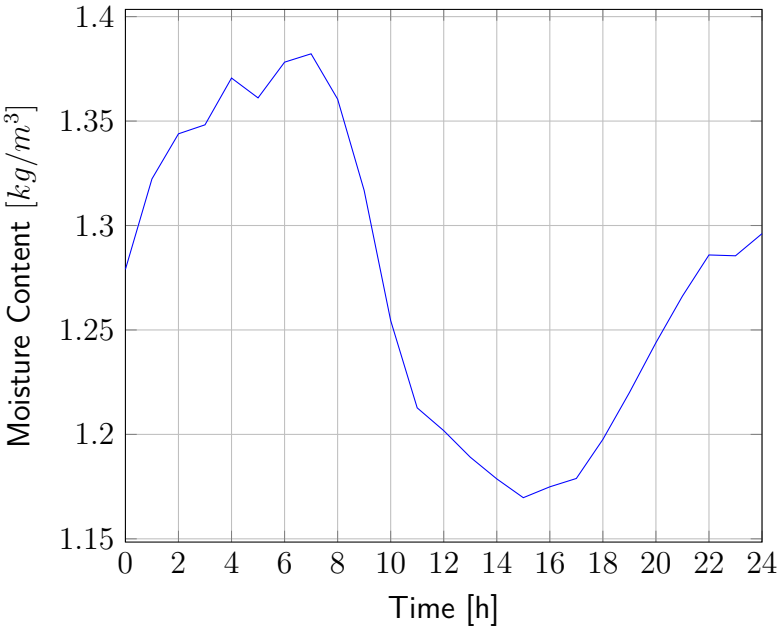

Figure 16: Moisture content evolution.

Fig.16 shows the moisture content series behavior during simulation. When the maximum negative flux occurs (almost 15 hours), the moisture content decreases due to evaporation. As seen in Fig. 15, the conduction heat transfer mode is the primary energy transport throughout PB and, even with the moisture content presence (with low variances), there is no sensitive changes over the general heat transfer, as noticed by the difference between the one found by Gasparini [39], with radiative and heat transfer effects accounted for, and the proposed model that includes a generic moisture storage function.

2.6 Final remarks

This paper presented an original mathematical formulation for predicting heat and moisture flow throughout porous bulding materials including the radiative heat transfer in scattering media such as fibrous insulation materials. The CAR-HAM model presented can solve problems of transport phenomena across building envelopes involving the three heat transfer modes, also considering the moisture adsorption/desorption and phase-change effects. At the moment, the main restriction of the proposed model is its application to unidimensional problems. The mesh can be treated by non-uniform distributions, according to the particular purposes. The Gaussian quadratures are changeable; however, the computer run time considerably increases with the number of points. Extensively verified with problem cases found in the literature, the proposed model has its consistency attested.

Some differences among the simulations with the proposed model and other models have been noticed, however the trends are very similar. The results submitted for the residential attic

show that insulation with high phenolic binder concentration is an excellent choice to reduce incoming heat flux. As shown, the proposed model provided results in good agreement. Some differences are attributed mainly to the lack of data for the radiation model.

A central challenge to apply more sophisticated models is the lack of material properties regarding both moisture and radiation phenomena. However, the results are not penalized, showing a stable and consistent method.

The differences found demonstrate the application of the model is promising and can be extended to domains where the radiative heat transfer through fibrous materials can play a more important role - such as in the industry of refrigeration, ovens and even airplanes, where gradients of temperatures are much higher than those commonly found in buildings.

2.7 Acknowledments

The authors acknowledge the Brazilian agencies CAPES of the Ministry of Education, and CNPq of the Ministry of Science, Technology and Innovation for the financial support.

3 Advanced building hygrothermal modeling

Abstract. *Moisture is one of the leading causes responsible for the worst of health conditions and energy performance in households and workplaces. To avoid it, the coupling between combined heat, air and moisture (HAM) model and a CFD code becomes a crucial for each topic to provide accurate results for real problems found in the building sector. Therefore, this paper presents a CFD-HAM model performed in one- and two-dimension simulations, displaying different results for each case. In the two-dimension example, the fluid flow is treated by Navier-Stokes with local convective heat and mass transfer coefficients calculated at the envelope internal surfaces and on the complicated surfaces as well. Two simulations are shown, where the the first one presents a wall with two thicknesses exposed to the ambient air with a turbulent flow where local heat and mass transfer coefficients along the surface are calculated. This simulation is led by a second one with a conditioning air system and one airflow complex obstruction (statue). A comparison between one- and two-dimension heat and mass transfer migration through plaster and brick - with trapped air - is carried out, showing the potential of the proposed advanced modeling to solve complex heat and moisture transfer in buildings.*
Keywords: *CFD-HAM; Navier-Stokes; two-dimension simulations.*

3.1 Introduction

Moisture in porous structures can significantly affect energy performance [49] and be also responsible for building pathology [24]. To predict those effects, research efforts since early nineties originated several hygrothermal simulation tools - such as DELPHIN [8], MATCH [9], MOIST [10], WUFI [11] and UMIDUS [12, 13] - and international projects in the frame of IEA Annexes 14, 24, 41 and 55 and the European project HAMSTAD. Their diffusion models are based on different driving potentials, as described in [14], enabling to predict better energy calculation through porous building materials. Nevertheless, models are commonly limited to the one-dimensional calculation (some to 2D) and assume a homogeneous convective resistance along the element geometry.

However, as shown in [50], a significant discrepancy may appear on corners if the convective heat and mass transfer coefficients are considered constant along the surface. Besides, most models do not simulate heat and mass transfer processes through complex geometries and are not integrated to air flow simulation despite the fact low-speed air circulation enables the accumulation of moisture. Moreover, thermal bridges and rising damp from the ground can considerably impact the hygrothermal building performance [7] and are not well precited by current tools. Besides those effects, moisture may deteriorate construction materials and affect building aesthetic appearance.

A detailed review of mathematical models, numerical methods, and simulation codes [14] show that among the ones that consider multidimensional diffusive transfer, a few take into account the external climatic conditions coupled with the porous medium, but a discrete model represents the external climate [51]; fewer, use some CFD package as a third part, and finally, rare models are combined to CFD, restricted to low humidity applications.

Airflow simulation in buildings has also been reported since the nineties, and the reader may refer to [7, 52–61] among many others. However, the differential formulation in the air domain coupled with moisture transfer has only been seen in [7]. Apparently, no work presents a way to solve problems where the heat and moisture effects are present in very non linear 3D problems, involving detailed surround air flow for the boundary conditions, considering its characteristics (laminar or turbulent), or even to calculate the local convective heat and mass transfer coefficient

throughout wall surfaces. With CFD-HAM those features are reached, enabling accurate results even for complex geometries.

The coupling with a CFD tool to solve complex problems - involving different geometries with accurate analysis of surrounding air by the solution of Navier-Stokes (NS) equations - is becoming nowadays more achievable thanks to the impressive development of hardware in the last twenty years.

The link between solid and fluid flow is not directly done, so it is important to use the governing equations for porous media to assess the correct transport of heat and mass by porous/fluid media interface. Besides, these equations take into account phase change and actively moisture dependent hygrothermal properties. The advantage of CFD coupling is to predict the fluid flow impact over the surface by convective heat and mass transfer. A poor airflow can promote mold growth, and the air convection becomes an important impact factor in the hygrothermal analysis, so it is essential to predict more accurately the convective and mass coefficients to not loose the accuracy of the diffusion models. Some research works present the convective heat transfer relationships based on measurements and specific conditions that represent the heat transfer coefficient at the corner [62]. About predicting mold growth, there are several works available in the literature [63–68]; however, the heat and the mass transfer coefficients are maintained constant all over the envelope surface, which may considerably understimate the mould growth risk.

Therefore, to accurately predict heat, air, and moisture (HAM) transport, this paper presents the integration of a HAM (Heat, Air and Moisture) model within a fluid dynamics tool – ANSYS–Fluent - so that to have HAM-CFD model to be applied to complex building elements, avoiding limitations such as homogeneous boundary conditions and without integration to air flow. The model employs the "used defined funtions" (UDF) available in the CFD package for the governing equations, considering moisture dependent properties. The model is then validated with a classical solution from literature [20] and simulations of complex problems, changing the geometries and boundary conditions, are presented to show the potentiality of this proposed code in the area of building physics.

This paper presents, in Section 3.2, the mathematical model, while the metodology and the model verification are presented in Sections 3.3 and 3.4. Section 3.5 shows results for complex cases and, finally in Section 3.6, conclusions are addressed.

3.2 Mathematical model

3.2.1 Conservation equations

The first goal of the present work is to comprise the following energy and moisture conservation equations in porous building materials into ANSYS-Fluent. The governing equations are described as follows:

$$\frac{\partial \omega}{\partial t} = -\nabla \cdot \left(-\delta_v \nabla P_v + \boldsymbol{u}\rho_v + \lambda \left(\nabla P_{suc} - \rho_l \boldsymbol{\xi}\right)\right) , \tag{34}$$

$$\frac{\partial H}{\partial t} = -\nabla \cdot \left(-k\nabla T + \boldsymbol{u}\rho_a c_a T + \boldsymbol{g}_v L_v + \boldsymbol{g}_l c_l T\right) - \nabla \cdot \boldsymbol{q}_{rad} , \tag{35}$$

where the total enthalpy can be described by:

$$H = \rho \left(c_o + \omega \frac{c_l}{\rho_o}\right) T , \tag{36}$$

where c_o is the specific heat of the porous material $[J/(kg \cdot K)]$, ρ_o, the specific mass $[kg/m^3]$, and c_l the specific heat of water $[J/(kg \cdot K)]$.

In Eq. (34), in the righ-hand side, the first term stands for the diffusion mass flow due to vapor pressure gradient, while the second one, for the convective vapor transport, and, the last term, for the liquid flow imposed by the suction pressure gradient. The energy conservation equation - Eq. (35), which represents the variation of total enthalpy with time, can be decomposed into five terms: heat conduction ($k\nabla T$), heat convection ($\boldsymbol{u}\rho_a c_a T$), phase change ($\boldsymbol{g}_v L_v$), sensible heat contribution due to the liquid flow ($\boldsymbol{g}_l c_l T$) and radiation ($\boldsymbol{q}_{rad}$). The radiation intensity contribution is important either on presence of higher temperatures or fibrous materials such as glass wool, but in this paper will be ignored.

Considering the moisture and energy conservation equations one can write:

$$Dp_1 \frac{\partial P_1}{\partial t} + Dp_2 \frac{\partial T}{\partial t} = \nabla \cdot \left(\Gamma^M_{P_1} \nabla P_1 + \Gamma_T \nabla T + \lambda \rho_l \boldsymbol{\xi} - \frac{\boldsymbol{u} M_l}{RT} P_1 J \right) , \tag{37}$$

for moisture and

$$\frac{\partial}{\partial t} \left[\rho \left(c_o + \omega \frac{c_l}{\rho_o} \right) T \right] = \nabla \cdot \left(\Gamma^E_{P_1} \nabla P_1 + (k + \Gamma^E_T) \nabla T + \lambda \rho_l \boldsymbol{\xi} c_l T - \frac{\boldsymbol{u} M_l}{RT} P_1 J L_v - \boldsymbol{u} \rho_a c_a T \right) \tag{38}$$

for energy. P_1 represents the variable to be used for the driving potential (either P_v or ϕ). The parameters used in Eqs. (37) and (38) are shown in Table 8, depending upon the choice of the driving potential.

	∇P_v	$\nabla \phi$
Dp_1	$\partial\omega/\partial\phi \cdot \partial\phi/\partial P_v$	$\partial\omega/\partial\phi$
Dp_2	$\partial\omega/\partial\phi \cdot \partial\phi/\partial P_{sat} \cdot \partial P_{sat}/\partial T$	$\partial\omega/\partial\phi \cdot \partial\phi/\partial P_{sat} \cdot \partial P_{sat}/\partial T$
$\Gamma^M_{P_1}$	$\delta_v + \delta_l(R\rho_l T/(M_l P_v))$	$\delta_v P_{sat} + \lambda(R\rho_l T/(M_l \phi))$
Γ^M_T	$\lambda(R\rho_l/M_l)(\ln\phi - (T/P_{sat})(dP_{sat}/dT))$	$\delta_v \phi(dP_{sat}/dT) +$ $\lambda(R\rho_l/M_l)(\ln\phi - (T/P_{sat})(dP_{sat}/dT))$
J	1	P_{sat}
Γ^E_T	$\Gamma^M_T c_l T$	$\delta_v \phi(dP_{sat}/dT) L_v T +$ $\lambda(R\rho_l/M_l)(\ln\phi - (T/P_{sat})(dP_{sat}/dT)) c_l T$
$\Gamma^E_{P_1}$	$\delta_v L_v + \lambda(R\rho_l T/(M_l P_v))L_l$	$\delta_v P_{sat} L_v + \lambda(R\rho_l T/(M_l \phi)) c_l T$

Table 8: Moisture and energy parameters for two different driving potentials.

3.2.2 Boundary conditions

The surrounding air is described by turbulence modelling considering the *k*-ϵ model that is based on model transportation equations for the turbulence kinetic energy *k*, and its dissipation rate ϵ. However, it needs to model air as a fluid in the CFD software, thus the simulation becomes much more costly due to additional mesh and the solution of the momentum conservation equation. For this reason, the fluid coupling was assumed only with the internal air. So, to calculate the relevant properties over internal porous material surfaces, it has been assumed the moisture at the region as follows:

$$(\boldsymbol{g}_v + \boldsymbol{g}_l)_{sur} = (\boldsymbol{g}_v + \boldsymbol{g}_l)_a \ . \tag{39}$$

Eq. (39) shows the vapor $\boldsymbol{g}_v$ and liquid $\boldsymbol{g}_l$ mass flow rates at the wall surface (sur) exchanging moisture with the ambient. The left-hand side refers to the mass flow at the internal wall surface,

while in the right-hand side the moisture from its the internal environment. On the right-hand side, $\boldsymbol{g}_l$ represents a liquid flow from the rain.

For the energy conservation equation, the balance at the surface can be expressed as:

$$(\boldsymbol{q}_{cond} + \boldsymbol{q}_{conv} + \boldsymbol{q}_{lat})_{sur} = (\boldsymbol{q}_{cond} + \boldsymbol{q}_{conv} + \boldsymbol{q}_{lat} + \boldsymbol{q}_{rad})_a \ , \tag{40}$$

where $\boldsymbol{q}_{cond}$ represents the heat conduction, $\boldsymbol{q}_{conv}$, the heat convection and, $\boldsymbol{q}_{lat}$, the latent heat due to the vapor-liquid phase change. This equation balance is applied at the external surface, and the rain load is neglected in the present work.

3.3 Methodology

In the CFD-HAM algorithm, the main equations were split to fill some internal commands for the macros of the CFD code [22]. Those macros are appropriately described in [69].

By means of ANSYS-Fluent user defined functions (UDF), considering the gradient of relative humidity as a driving potential, the boundary conditions were rewritten as follows:

$$\left[-\Gamma_{P_1}^{M} \nabla\phi J + \frac{\boldsymbol{u} P_{sat}}{R_v T}\phi - \lambda\rho\boldsymbol{\xi}\right]_{sur} = (\boldsymbol{g}_v)_a \, , \tag{41}$$

where,

$$(\boldsymbol{g}_v)_a = \left[\vartheta \boldsymbol{\Delta} P + \frac{\boldsymbol{u}\ P_v}{R_v T}\right]_a \, . \tag{42}$$

In Eq. (41), the right-hand side term represents the moisture flow coming from the internal environment. The first part is the diffusive moisture flow, while the second one represents the convective part.

In the left-hand side, the $\Gamma_{P_1}^{M}$ stands for the diffusivity of the material. For its calculation, the ANSYS-Fluent code provides the diffusive scalar flux by evaluation of two gradients: along directions that connect cell centroids and along the face direction plane. So, after some rearrangements, Eq. (41) can be rewritten as:

$$\phi_{sur} \cdot \left[\frac{\Gamma A_{be}}{d_r} + \left(\vartheta + \frac{\boldsymbol{u}}{R_v T}\right) P_{sat} \boldsymbol{A}\right]_{sur} = \frac{\Gamma A_{be}}{d_r}\phi + \left[\left(\lambda\rho_l\boldsymbol{\xi} + P_v\left(\vartheta + \frac{\boldsymbol{u}}{R_v T}\right)\right)\boldsymbol{A}\right]_{sur} - \beta_o \, . \tag{43}$$

In Eq. (43), in the left-hand side, d_r stands for the distance between adjacent cells, A the surface area and the A_{be} the areas relationship into primary flux diffusion between cell centroids according to direction $\boldsymbol{e}_s$:

$$A_{be} = \frac{\boldsymbol{A} \cdot \boldsymbol{A}}{\boldsymbol{A} \cdot \boldsymbol{e}_s} \, . \tag{44}$$

The term β_o refers to the cross diffusion by the follow equation:

$$\beta_o = \Gamma_{sur} \left(\bar{\nabla}\phi \cdot \boldsymbol{A} - \phi \cdot \boldsymbol{e}_s A_{be}\right) \, . \tag{45}$$

The term $\bar{\nabla}\phi$ represents the average of the gradients in two adjacent cells.

To calculate the relative humidity at the internal surface, the short form of Eq. (43) is represented by:

$$\phi_{sur} = \frac{\gamma_1}{\gamma_2}\phi + \frac{\gamma_3}{\gamma_2} \, , \tag{46}$$

where,

$$\gamma_1 = \frac{\Gamma}{d_r} A_{be},$$
$$\gamma_2 = \gamma 1 + \left(\vartheta + \frac{\boldsymbol{u} M_l}{RT}\right) P_{sat} \boldsymbol{A}_{sur},$$
$$\gamma_3 = \left[\left(\vartheta + \frac{\boldsymbol{u} M_l}{RT_a}\right)(P_v)_a + \lambda \rho_l \boldsymbol{\xi}\right] \boldsymbol{A}_{sur} - \beta_o.$$

The energy balance equation on surface operates similarly to the moisture calculations. Then, after some rearrangements of Eq. (40), the internal surface temperature T_{sur} is obtained by:

$$T_{sur} = \frac{\gamma_1}{\gamma_2} T + \frac{\gamma_3}{\gamma_2}\,, \tag{47}$$

where,

$$\gamma_1 = \frac{\Gamma}{d_r} A_{be},$$
$$\gamma_2 = \gamma 1 + (\upsilon_h + \boldsymbol{u} \rho_a c_a) A_{sur},$$
$$\gamma_3 = [(\boldsymbol{u} c_a + \upsilon_h) T_a + (\boldsymbol{g}_v)_a \; L_v - (\boldsymbol{g}_v L_v + \boldsymbol{g}_l c_l T)_{sur}] - \beta_o\,.$$

3.4 Model verification

With the aim of verifying the CFD-HAM performance, a simulation of the homogeneous wall was submitted to the surrounding air with its relative humidity lower than the one within the wall porous structure. The moisture and heat transfer occurs through the homogeneous wall, with no air pressure difference, under isothermal conditions. The main data is described in Table 9. Further details can be found in [20], Benchmark 2.

Sorption isotherm (ω)	$116 \cdot (1 - ln\phi/0.118)^{0.869}$	kg/m^3
Vapour diffusion (δ_v)	$1.0 \cdot 10^{-15}$	s
Moisture diffusivity (D_l)	$6.0 \cdot 10^{-10}$	m^2/s
Thermal conductivity (k)	0.15	$W/(mK)$
Specific heat capacity (c_o)	800	$J/(kgK)$
Density (ρ_o)	525	kg/m^3
Thickness (e)	0.2	m
Latent heat (L_v)	56.8	J/kg
Convective mass transfer coeff. (ϑ)	$1.0 \cdot 10^{-3}$	s/m
Convective heat transfer coeff. (υ_h)	25	$W/(m^2K)$
Temperature (T) (internal and external)	293.15	K

Table 9: Simulation data - homogeneous wall.

So, the moisture and heat into/out the wall can be described as follows:

$$\boldsymbol{g}_v = \pm \vartheta \boldsymbol{\Delta} P_v + \frac{\boldsymbol{u} P_a}{R_v T_a}\,, \tag{48}$$

$$\boldsymbol{q} = \pm \upsilon_h \boldsymbol{\Delta} T + \boldsymbol{u} \rho_a c_a T_a + \boldsymbol{g}_l c_l T + \boldsymbol{g}_v L_v, \tag{49}$$

where ϑ and υ_h represent the surface convective coefficients of water vapor and heat transfer. Their values are given in the original simulation as 0.001 s/m and 25 $W/(m^2 \cdot K)$. Simulation results from CFD-HAM and Others[2] are displayed in Fig. 17.

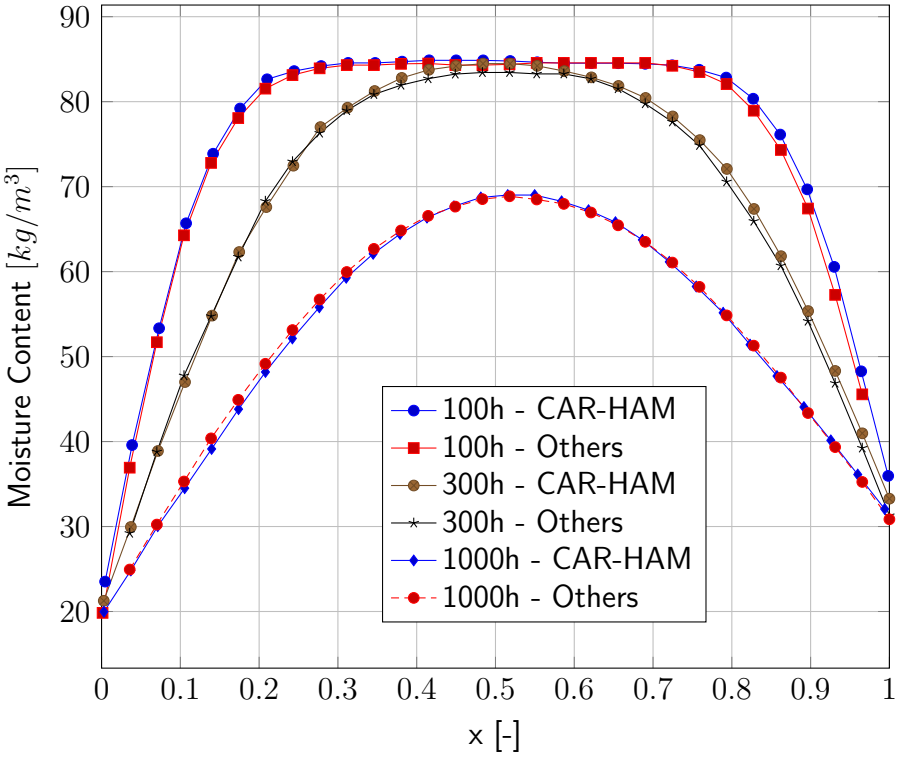

Figure 17: Homogeneous wall - predicted moisture content.

3.5 Results

In this section, we first discuss the importance of calculating the heat and mass convective coefficients and their coupling with the surrounding air. For example, the distribution of temperature and moisture content within a L-shaped wall is shown influenced by a complex airflow. The convective transfer coefficient profiles are also presented.

Then, a more complicated case is presented for an air-conditioned museum space with a statue positioned near the wall. The air conditioner is assumed to supply air at a constant set-point temperature. In this example, the proposed model computes the temperature distributions within the three physical domains: air, wall, and statue. It was considered that the wall and the statue are made of materials with different higroscopicity, and because of this, the moisture distribution presented very different values.

Finally, a comparison between 1D and 2D models is presented, showing the main differences in the approaches, especially regarding the treatment given in the fluid domain.

In a real case, convective heat and mass transfer coefficients are non-uniform. In this way, it is necessary to consider the airflow as a boundary condition. The $k - \epsilon$ turbulence model

[2]Others represent the solutions obtained by the following institutes and universities: KUL (University of Leuven), TECHNION (Technion Israel Institute of Technology), TUD (Technical University of Dresden), CTH (Chalmers University of Technology), NRC (National Research Council of Canada) and IBP (Fraunhofer Institute of Building Physics). More details can be found in [20].

was choosen for this work due to its reliability and computational efficiency [70]. On the other hand, $k-\omega$ turbulent model is recommended to low Reynolds numbers and its precision is better closer to the wall, but the convergence, and accuracy of this turbulence model may not be high for free flows [71]. Thus, the link between porous and surrounding fluid flow is given by some dimensionless numbers. The calculation of Reynolds, Schmidt, and Sherwood numbers define the mass transfer coefficient; Reynolds, Prandtl and Nusselt are used to obtain the convective heat transfer coefficient. Eqs. (50) and (51) provide the solution to get those convective coefficients [72]:

$$\upsilon_m = \psi \left(\frac{\mu}{\rho_a D}\right)^{\frac{1}{3}} \left(\frac{\rho_a \boldsymbol{u} \iota}{\mu}\right)^{\frac{1}{2}} D/\iota, \tag{50}$$

$$\upsilon_h = \psi \left(\frac{\mu}{\alpha}\right)^{\frac{1}{3}} \left(\frac{\rho_a \boldsymbol{u} \iota}{\mu}\right)^{\frac{1}{2}} k_l/\iota. \tag{51}$$

In Eqs. (50) and (51), the constant ψ depends on fluid flow (laminar or turbulent), μ is viscosity, ρ is the specific mass, D is the mass diffusivity, $\boldsymbol{u}$ is the fluid flow velocity, α is the thermal diffusivity and, finally, ι is the characteristic lenght.

Considering the boundary conditions according to Eq. (39) and, applying the simulation described in section 3.4 to a bidimensional case, as illustrated in Figs. 18 and 19. Fig. 18 also provides the temperature distribution over the wall. The geometry is slightly different and smooth isotherm lines at the top of the wall are observed. The convective heat transfer coefficient has a high dependency of fluid flow characteristics, mainly its velocity. The internal temperature was considered constant. The internal ambient has an inlet flow with speed of $1m/s$. Fig. 19 shows the air velocity and moisture content profiles within the wall for the same physical problem seen in Fig. 18.

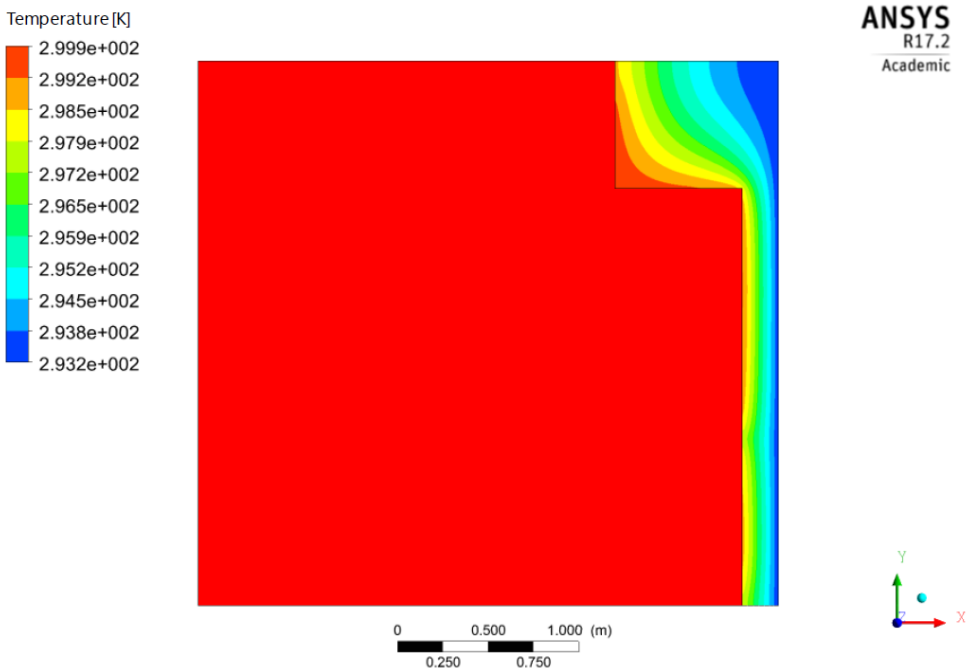

Figure 18: Predicted temperature profile within the wall.

The vapor pressure gradient drives the diffusion of moisture within the wall and over its surface, by advective movement of airflow. The moisture exchange is highly air velocity dependent. Although the airflow is laminar due the low air speed, important values of convective heat and

mass transfer coefficients appear as shown in Figs. 20-25. The air circulation shows the direct effect of its velocity on convective heat and mass transfer coefficients. For instance, in Fig. 25, the heat transfer has the major value at y equal to 0.5 m. In Fig. 19, at surface "S3", the local air velocity promotes a great exchange of heat and mass between the porous material and the surrounding fluid. On the other hand, in the same Fig. 19, at low corner indicated by point "A", poor air circulation decreases heat and mass transfer as seen in Figs. 24 and 25, around y = 1.5 m.

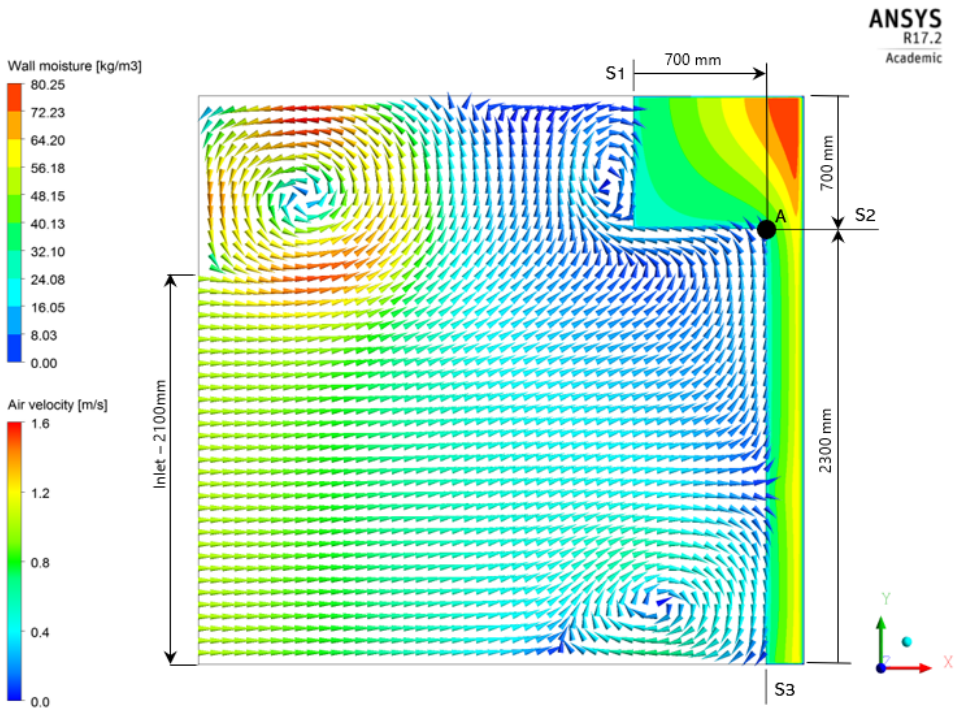

Figure 19: Predicted moisture within the wall and air velocity.

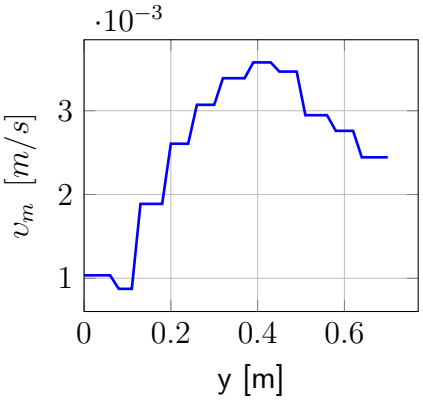

Figure 20: Predicted convective mass transfer coefficient at the surface "S1".

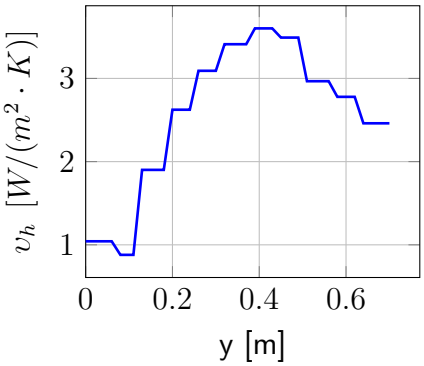

Figure 21: Predicted convective heat transfer coefficient at the surface "S1".

The simulation code coupled with the CFD package becomes a powerful tool. If the aim is to provide a simulation with more real details, the present problem can be changed to a more complicated case, for instance, a study of a hygrothermal behavior of a statue in a museum room as shown in Fig. 28. The wall properties were presented in [20], benchmark 2, and the statue property is described in [20], benchmark 4 (internal material). The inlet air velocity of the air

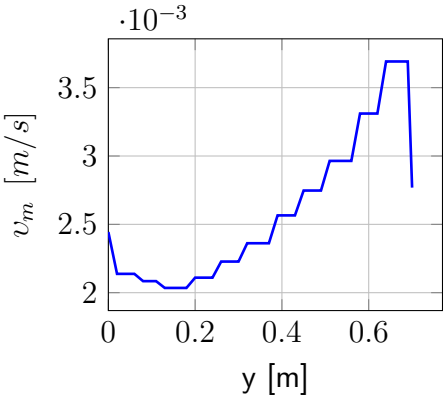

Figure 22: Predicted convective mass transfer coefficient at the surface "S2".

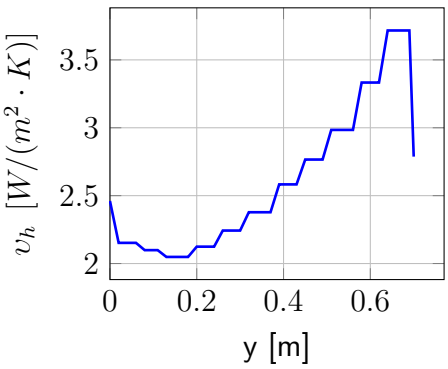

Figure 23: Predicted convective heat transfer coefficient at the surface "S2".

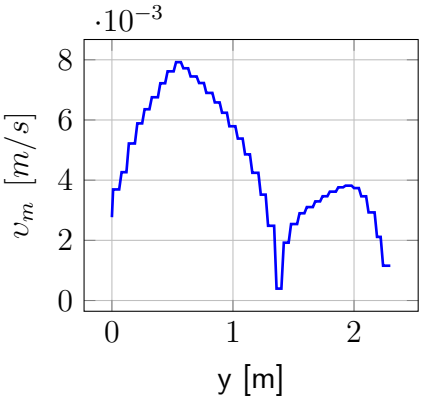

Figure 24: Predicted convective mass transfer coefficient at the surface "S3".

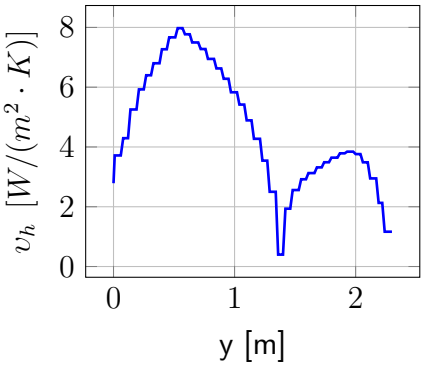

Figure 25: Predicted convective heat transfer coefficient at the surface "S3".

conditioning system was set to 1 m/s. Initially, the walls, the ambient (indoor and outdoor) and the plaster statue presents a temperature of 300K and 95% of relative humidity; the air conditioning inlet is at 290K. A uniform mesh (5 mm^2 and 30 mm^2) is used for brick and air trapped in the cavities, respectively, for the two-dimensional simulation (see Fig. 26). In Fig. 27, it is shown the refined mesh used for statue and walls. The time step starts with 0.01 s and, after 200 iterations, it is increased to 1 s, with a simulation period of 480 h.

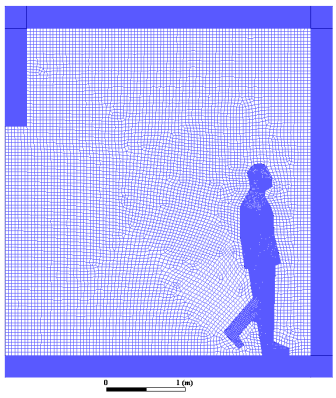

Figure 26: Mesh used for the museum room simulation.

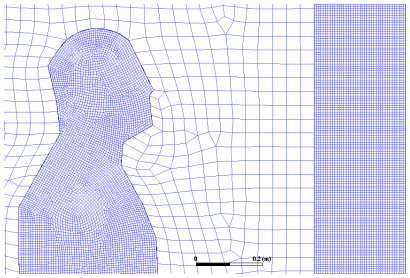

Figure 27: Statue and walls mesh details.

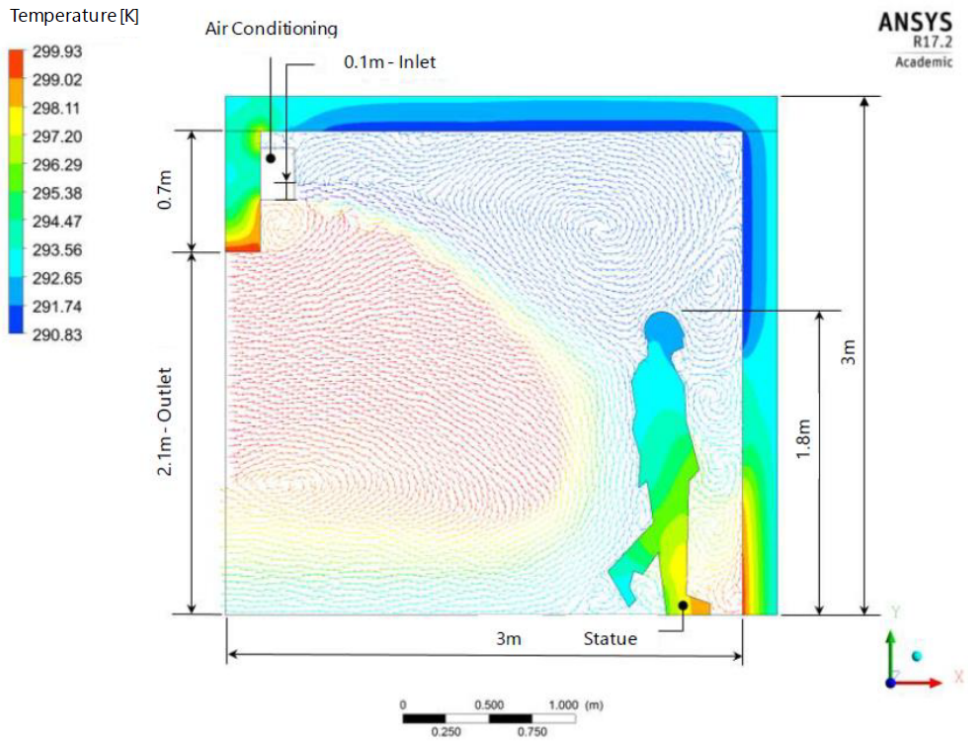

Figure 28: Temperature distributions within different physical domains: air, wall and the plaster statue.

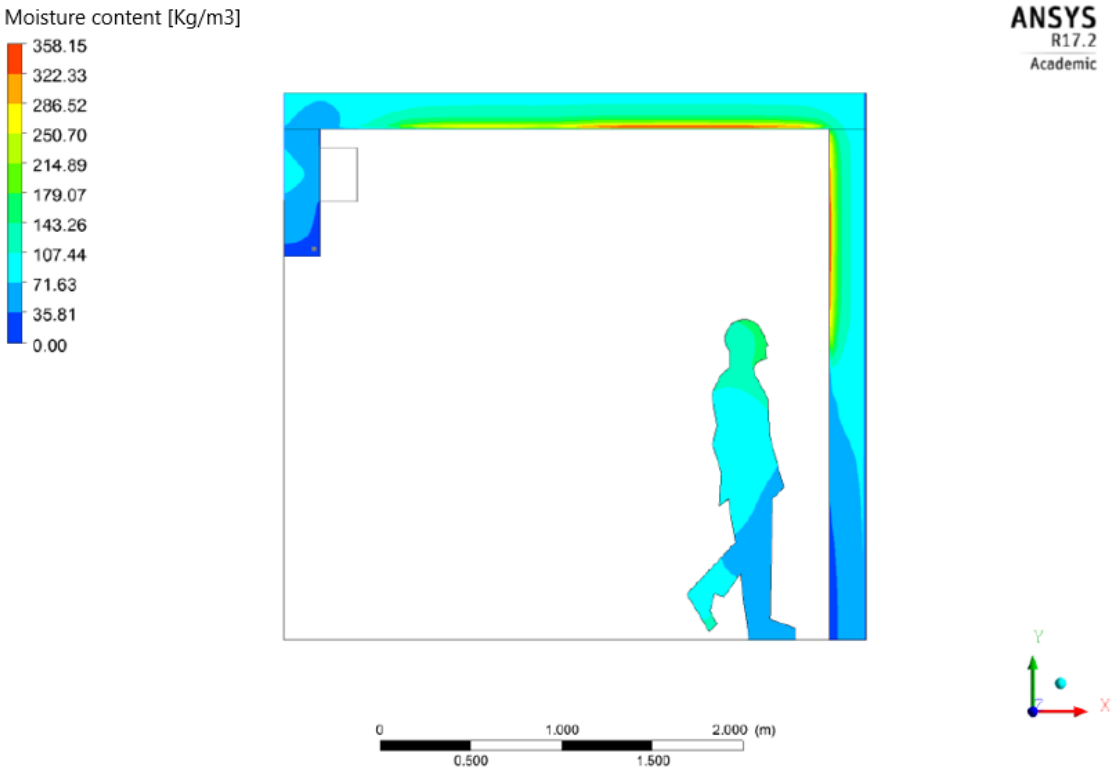

Figure 29: Moisture content distribution within the wall and the plaster statue.

Fig. 28 represents a gallery wall where fluid flow from air conditioning impinges the plaster statue near the wall. It is possible to see the air circulation at the ambient and the temperature

distribution as well. The upper left corner has a substantial temperature difference (5 K), and at the top right corner it shows lower temperature achieving a large part of the top and right walls with high moisture content concentration, as shown in Fig. 29.

The plaster statue has its base with low moisture content due to poor air movement. At the top, the water content is greater. The local air circulation promotes a high heat transfer coefficient; however, the mass flow of the air is also carried into the structure; Eq. (50) gives the relationship between air velocity and the mass coefficient, implicitly represented by the Reynolds number. According to the boundary condition in Eq. (48), the mass flow is influenced by the airflow. In Figs. 28 and 29, it can be observed the regions where the temperature is greater, the humidity is low; the opposite is also true.

Combining heat and moisture transfer through porous media in one-dimensional gives often a fast solution for hygrothermal analyses. Nevertheless, it may become insufficient to represent physical problems, for instance, hygothermal bridges. Due to its characteristics, this kind of problem needs to consider mass and heat transfer in more than one direction; even though for a building construction element, such as a brick, moisture, and heat transfer in one direction assumption may not be conclusive. Aiming to compare one- and two-dimensional approaches, simulation of heat and moisture migration across a multilayered wall is presented regarding relative humidity and temperature distributions. A wall composed of plaster, brick, and air (see Fig. 30) is now considered to compare the 2D effect of an advanced model (CFD-HAM). The hatched area represents the 1-D range. In this case, air layer is described as a porous material as proposed in [11]). Thus, vapor flow can be obtained by:

$$\boldsymbol{g}_v = -\frac{\delta_v}{\mu}\nabla\phi \ . \tag{52}$$

In Eq. (52), δ_v represents the concentration-related diffusion coefficient in the air $[m^2/s]$ and μ represents the effective resistance factor to water vapor diffusion. It has high a thermal dependence as shown in Eq. (53).

$$\delta_v = \left(2.1 \cdot 10^{-7}\right)\frac{T^{0.81}}{P_a} \ , \tag{53}$$

where T means the temperature $[K]$ and P_a, the atmospheric pressure $[Pa]$.

A linear relationship describes the moisture storage function $[kg/m^3]$ as follows:

$$w = 0.017\phi, \tag{54}$$

where ϕ stands for the relative humidity $[-]$. Those air properties are validated for a 30 cm layered air, according to the WUFI material data base. The temperature used for the simulation was 273 K (see Tables 10, 11 and 12 for further details on simulation data).

A comparison between one- and two-dimensional simulations at t = 6 h, for temperature, moisture content and relative humidity distributions, show some differences in the solution. In Fig. 31, the CAR-HAM[3] model has its distributed values of temperature slightly higher than WUFI simulation. The temperature in the middle of the brick has a peak for the 2D case, represented by the CFD-HAM model, and this occurs due the to area insulated by the air cavity. A low heat transfer increases the temperature. With the one-dimensional approach, this fact cannot be observed. In Fig. 32, 1D and WUFI models present a continuous moisture content within the brick, which was somewhat different for the CFD-HAM results. In fact, a high temperature in the middle of the block prevents a moisture increase.

[3]CAR-HAM is a **C** code written to solve the proposed mathematical model in one dimension by using fully implicit scheme and the MTDMA [12].

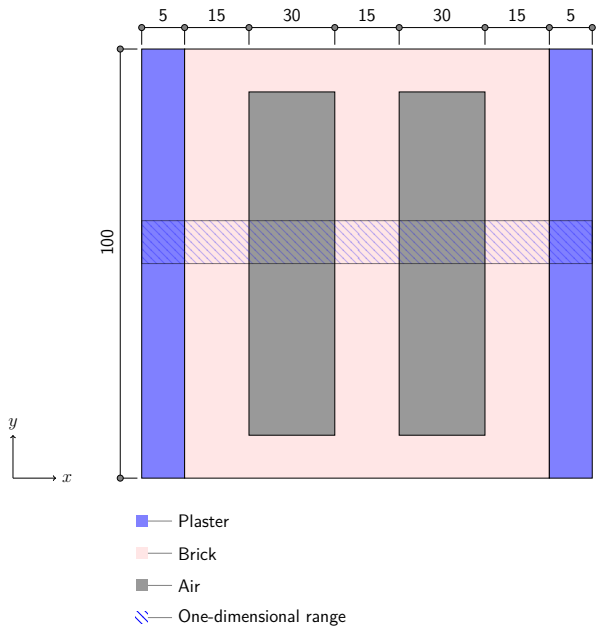

Figure 30: Brick: two-dimensional approach - unit in mm.

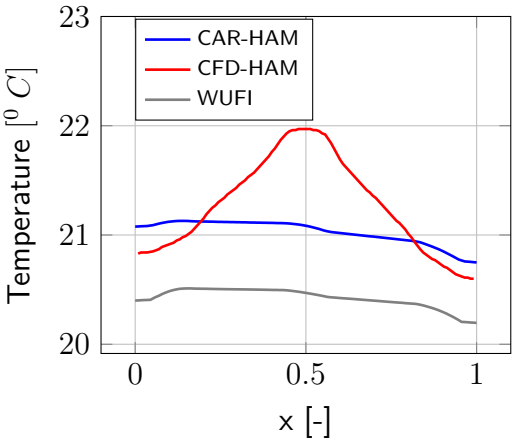

Figure 31: Predicted temperature.

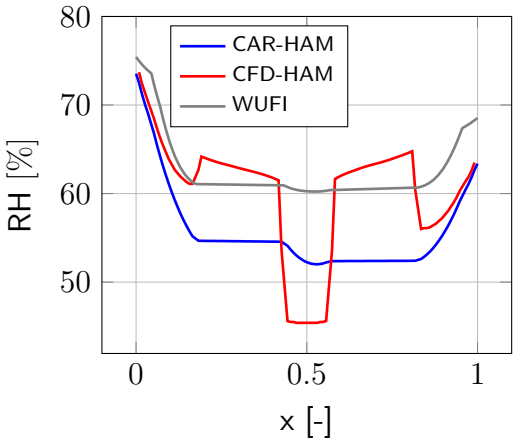

Figure 32: Predicted relative humidity.

In Fig. 33, all models have similar results, even though with temperature differences in the region because the moisture content is dependent on the capillary pressure. However, the simulation period was not long enough to show a significant change on the moisture content distribution.

An essential contrast amidst all results: for a 1-D assumption, the air layer is considered as a solid with equivalent fluid properties and, in 2-D, it is treated as a fluid. The flow field with natural buoyancy forces is not represented by the 1D approach. Besides, only the CFD-HAM model can show a non-symmetric temperature distribution (see Fig. 34).

The convective heat transfer coefficient $[W/(m^2K)]$, and the convective mass transfer coefficient $[m/s]$ have their local values at interface between solid and air trapped within cavities calculated considering the buoyancy effects. The convective mass transfer coefficient is given by Eq. (50), and the Reynolds number (R_e) considering the buoyancy forces, is obtained by:

$$R_e = R_{ay}^{-\frac{1}{4}} \cdot P_r, \tag{55}$$

where P_r stands for the Prandtl number, and R_{ay}, for the Rayleigh number that is described by:

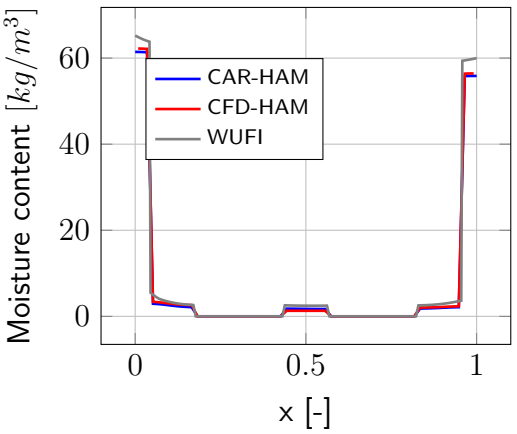

Figure 33: Predicted moisture content.

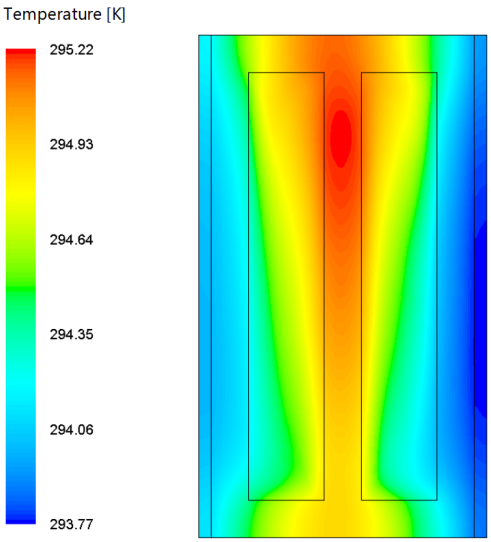

Figure 34: Predicted temperature within the multilayered wall.

$$R_{ay} = GP_r. \tag{56}$$

For the simulation, the Grashof number G (the ratio between the buoyancy force and the viscous force) has the value of $(1 \cdot 10^9)$, which represents the parameter to describe the laminar (lower values) or turbulent flow (higher values).

The heat flux at the internal wall cavities depends on the convective heat transfer coefficient $[W/(m^2K)]$ as follows:

$$\upsilon_h = \frac{N\ k_l}{\iota}. \tag{57}$$

In Eq. (57), k_l represents the thermal conductivity $[W/(mK)]$. The Nusselt number (N) may be defined according to the internal cavity ratio, that is the relationship between height ι and width B $[m]$, as follows:

$$r = \iota/B. \tag{58}$$

So, the Nusselt number can be written according to the r value [72]:

$$N = 0.22\left[\left(\frac{P_r}{0.2+P_r}\right)R_{ay}\right]^{0.28} + r^{0.09} \quad r > 2, \tag{59}$$

else

$$N = 0.18\left[\left(\frac{P_r}{0.2+P_r}\right)R_{ay}\right]^{0.29} + r^{-0.13} \quad r \leq 2. \tag{60}$$

Taking into account Equations 52 to 60 had influence over assymetric temperature distribution showed in Fig. 34. As seen, for the internal cavities of brick, due to the natural convection, several mathematical operations are needed to calculate the heat and moisture exchanges at the solid/fluid interface. All this does not make sense for one-dimensional simulation, which explains the differences presented in Figs. 31 and 32.

Brick		
Sorption isotherm (ω)	$871 \sum_{i=1}^{2}\ k_i/(1+(a_i\ h(P_{suc}))^{n_i})^{m_i}$	kg/m^3
Vapour diffusion (δ_v)	$c_1 c_2/c_3$	s
Liquid water conductivity(λ)	$exp(\sum_{i=0}^{5}\ a_i(\omega/\rho_l)^i)$	s
Thermal conductivity (k)	$0.06 + 0.56(\omega/\rho_l)$	$W/(mK)$
Specific heat capacity (c_o)	1000	$J/(kgK)$
Density (ρ_o)	212	kg/m^3
Thickness (e)	0.105	m
Plaster		
Sorption isotherm (ω)	$209(1 + c_5)^{c_4}$	kg/m^3
Vapour diffusion (δ_v)	$c_1 c_6/c_7$	s
Liquid water conductivity(λ)	$exp(c_{14})$	s
Thermal conductivity (k)	$0.2 + 0.0045\omega$	$W/(mK)$
Specific heat capacity (c_o)	870	$J/(kgK)$
Density (ρ_o)	790	kg/m^3
Thickness (e)	0.005	m

Table 10: Hygrothermal properties - multilayered wall.

Mass transfer coefficient (ϑ) (internal / external)	$1.85 \cdot 10^{-8}/9.25 \cdot 10^{-8}$	s/m
Heat transfer coefficient (υ_h) (internal / external)	$10/10$	$W/(m^2K)$

Table 11: Convective mass transfer coefficients - multilayered wall.

Brick	
c_1	M_l/RT
c_2	$(26.1 \cdot 10^{-6}/\mu)(1-(\omega/871))$
c_3	$(0.8)(1-(w/871))^2+0.2$
Plaster	
c_4	$0.27/1.27$
c_5	$(2 \cdot 10^{-6} P_{suc})^{c_4}$
c_6	$(26.1 \cdot 10^{-6}/3)(1-(\omega/209))$
c_7	$(0.503)(1-(\omega/209))^2+0.497$
c_8	0.0704
c_9	$1.742 \cdot 10^{-4}$
c_{10}	$2.7953 \cdot 10^{-6}$
c_{11}	$1.1566 \cdot 10^{-7}$
c_{12}	$2.5969 \cdot 10^{-9}$
c_{13}	$\omega - 120$
c_{14}	$-33.0 + c_8 c_{13} - c_9 c_{13}^2 - c_{10} c_{13}^3 - c_{11} c_{13}^4 + c_{12} c_{13}^5$

Table 12: Parameters.

3.6 Final remarks

The proposed methodology represented by the CFD-HAM model brings a powerful hygrothermal tool that enables to solve a wide spread of problems that involve the surrounding air described by Navier-Stokes equations combined to multidimensional diffusion phenomena. Besides, it is possible to account for the dimensionless numbers such as Reynolds and Nusselt, aiming to provide local convective heat and mass transfer coefficients, instead of a constant ratio to the entire wall. Therefore, moisture and temperature fields are driven by the airflow characteristics (laminar or turbulent), providing the real influence of boundary conditions. Regions with poor air circulation, like corners, might easily promote moisture accumulation, which can not been predicted by conventional moisture models that are not coupled with codes to solve the mass, energy and momentum balance equations in the air domain.

The interface between air and building envelope is not necessarily linear, which gives the possibility of considering non-flat surfaces. In a real case simulation, several assumptions or choices determine the problem solutions. The comparison between one and two-dimensional simulation showed important differences (see Figs. 31 and 32). With the 1D approach, both temperature and moisture content distributions present worse accuracy than 2D approach, mainly in air zone modeled as a porous zone. However, one-dimensional simulation has produced reasonable results despite its restrictions since a fluid flow cannot be appropriatelly modelled in 1D.

To conclude, the CFD-HAM model provides a way to analyze many situations with complex surfaces solving a large part of complex problems in the building sector, calculating local values of heat and mass fluxes, involving moisture and temperature migration in buildings or in complex porous building elements.

Although the high power of such a tool, the computer run cost is still a grave concern to make it usable in whole-building annual hygrothermal analyses. In this way, further research must

be conducted to drastically reduce the computer runtime. A possible solution might be based on the method presented by Mazuroski et al. [53], adapting it to the moisture transfer problem.

3.7 Acknowledgments

The authors acknowledge the brazilian agencies CAPES of the Ministry of Education, and CNPq of the Ministry of Science, Technology and Innovation. This study was financed in part by the Coordenação de Aperfeiçoamento de Pessoal de Nível Superior - Brasil (CAPES) - Finance Code 001. The authors also acknowledge the ESSS (ESSS Institute for Education, Research and Development) and ANSYS for the technical and research support.

4 Assessment of Advanced Hygrothermal Modeling

Abstract. *An experimental set-up according to a Nordtest protocol, where a plywood box is exposed to cycles of moist air in an isothermal environment, whose objective is rating its moisture buffer value index (MBV), which represents the rate between mass variation and relative humidity changes. Relative humidity and water content distributions in the plywood box with MBV index calculation are presented using two mathematical models. The first one, called CAR-HAM (Conductive, Advective, and Radiative Heat, Air and Moisture) is a one-dimensional model where the main governing equations of moisture and energy are solved by MTDMA algorithm using a fully implicit scheme. The second model (CFD-HAM) represents the CAR-HAM model rewritten for multidimensional applications and, it is fully coupled with the CFD commercial package ANSYS-Fluent.The two proposed models provided results in close agreement with experimental data, with a relative error below 5%.*
Keywords: *Nordtest,moisture validation, MBV,CAR-HAM, CFD-HAM.*

4.1 Introduction

In the building sector, the control of relative humidity in indoor environments has been the object of several research studies in the last three decades. The heat and mass transfer mechanisms that promote the exchange of internal air humidity with the porous building material involve several parameters such as air velocity in the environment, relative humidity, and microestructure of the porous building elements. The employment of porous material with its hygroscopic behavior that promotes sorption/desorption of moisture may improve the hygrothermal comfort, attenuating relative humidity variations and may reduce energy consumption with systems of air conditioning [9]. In this way, Padfield [73] suggested the use of hygroscopic materials to the humidity control. In museums, for instance, moisture may cause several damages and a strict control of relative humidity (RH) is mandatory. Low and high values of relative humidity should be avoided, preventing dehydration, material deterioration, mold growth risk, condensation risk and health problems. In metals, higher humidity may lead to corrosion. It is not an easy task to simplify a complex physical phenomenon related to the process of mass transfer [74], but some authors tried to standardise the moisture migration to/from porous material [75, 76], but only in 2003, the moisture buffer value (MBV) index was provided by Rode [9].

The Danish Technological University, the Technical Research Centre of Finland, the Lund University, and the Norwegian Building Research Institutes created a Nordtest protocol to evaluate the MBV performance and, the results obtained by these institutions had a good agreement for standardization purposes. In this way, some experimental tests were conducted at the Thermal System Laboratory at the Pontifical Catholic University of Parana - PUCPR, in 2007 [77] and later, in 2017 a smaller test-cell replied the same experimental setup [78]. In 2017 a mathematical model simulated the experimental test in the laboratory [79]. The results of the measurements and numerical model presented some divergences due to uncertainties over the acquisition data system and the material properties used in the simulations.

With the objective of reaching the best results of previous numerical codes and lab. results, the present work introduced the new mathematical model coupled to the CFD software (ANSYS-Fluent) [22] called CFD-HAM to simulate the lab. experimental set-up considering the Nordtest protocol. The energy and moisture conservation equations described in this simulation code compute the moisture content, relative humidity, and mass flow exchanged with the plywood panel to calculate the effective MBV index.

4.2 Experimental Set-up

A test-cell designed and built by Silva [78] (following Meisner work [77,80]) is composed of a wooden structure to mechanically support the plywood box (see Fig. 35). The wooden support is waterproofed with aluminium foil to avoid moisture migration. The test cell is composed of six plywood panels with 15 mm of thickness, in which both width and height measure 860 mm. The air flow (0.115 m/s) blows into the plywood box by the inlet hole and flows out by the outlet hole as shown in Fig. 35. Temperature and humidity probes are located at the inlet, outlet and in the midlle of the plywood box. The experimental apparatus is exposed to relative humidity changes from 33% (for 16 h) to 75% (for 8 h), according to the Nordtest protocol. The controlled air mass flow rate comes from a supply air handling unit that controls the desired supply air temperature and relative humidity [77].

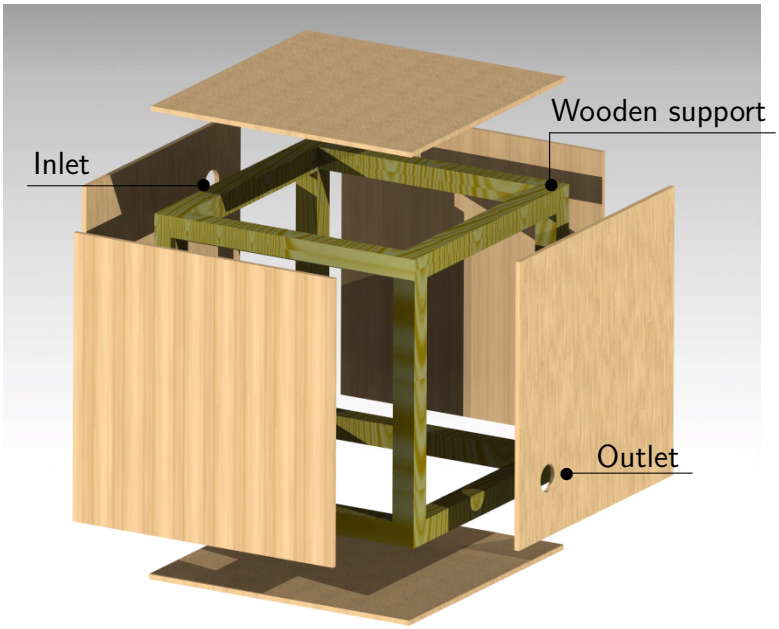

Figure 35: Experimental apparatus for MBV index assessment.

The MBV index was measured for the plywood box indicated in Fig. 35. The moisture buffer value is related to the amount of water transported to/from the porous media per unit of area, with moisture variation during a certain period. The box is exposed to a high relative humidity (RH) of 75% for 8 hours and 33% RH for 16 hours, and repeated for at least three times while the mass variation for each cycle respect the upper limit of 5%. The test cell weight changes consider the difference of the sorption and desorption of water in the material. So, the MBV $[kg/(m^2\%RH)]$ is calculated by the mean of the last three measurements [9] and can be described by:

$$MBV = \frac{\Delta m}{A \cdot \Delta \phi}, \tag{61}$$

where m represents the mass (kg), A stands for the area (m^2) and ϕ is the relative humidity.

A high MBV index indicates a suitable material to attenuate more significantly the relative humidity. Fig. 36 displays the MBV classification [9].

The test-cell (see Fig. 35) measurements presented an MBV index of 5.95 [78]. These results were distinct from past simulation code [79].

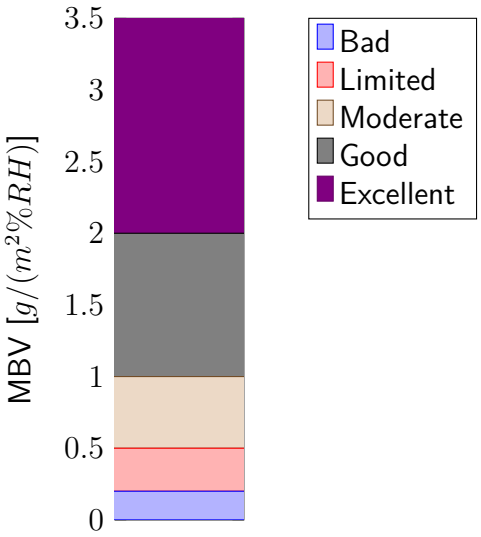

Figure 36: MBV index rating ref.[9].

4.3 Numerical

The CFD-HAM model solves the energy and mass governing equations for the porous material domain as:

$$\frac{\partial \omega}{\partial t} = -\nabla \left(\boldsymbol{g}_{tot} \right), \tag{62a}$$

$$\frac{\partial T}{\partial t} + \nabla \left(\boldsymbol{u} \rho_a c_a T \right) = -\nabla \left(k \nabla T + \boldsymbol{g}_v L_v + \boldsymbol{g}_w c_w T \right). \tag{62b}$$

Equations (62a) and (62b) represent the moisture and the energy balances within the porous medium. The first one describes the water content $[kg/m^3]$ accumulation during the time that depends on the moisture flux divergent $[kg/(m^2 s)]$. In Eq. (62b), one can see the temperature changes on time (first left-hand term, the transient term) are due to advection (second left-hand term), heat diffusion (first right-hand term) and phase change (second and third right-hand terms).

The main equations were splited to fill up the user defined functions (UDF), which are predefined macros provided by the CFD software (see Table 13).

Macros	Function
DEFINE DELTAT	controls the variable time step;
DEFINE ADJUST	the main macro to calculate the variables for each iteration;
DEFINE INIT	used to specify initial conditions;
DEFINE UDS UNSTEADY	used to calculate the unsteady terms;
DEFINE PROPERTY	defines the material or fluid properties;
DEFINE DIFFUSIVITY	used to determine the diffusivity terms;
DEFINE SOURCE	used for the source terms;
DEFINE PROFILE	used for boundary conditions.

Table 13: ANSYS-Fluent Macros used in the CFD-HAM model.

Ansys-Fluent was set-up to solve the governing equations by its pressure-based solver that is a numerical method for low-speed incompressible flows. It is employed the finite-volume

technique [22] and the $k-\epsilon$ model [70]. The test-cell sketch built in the CFD software (see Fig. 39) considers a Cartesian $1mm^2$ uniform mesh with 110.000 elements as shown in Fig. 37. A refinement of the mesh in the interface can be seen in Fig. 38.

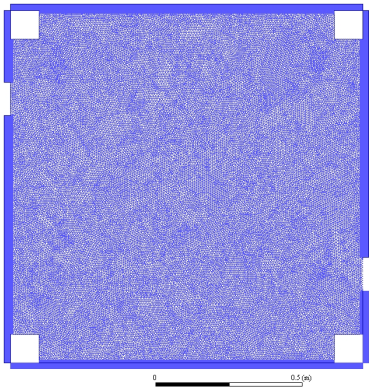

Figure 37: Plywood mesh used for the simulation.

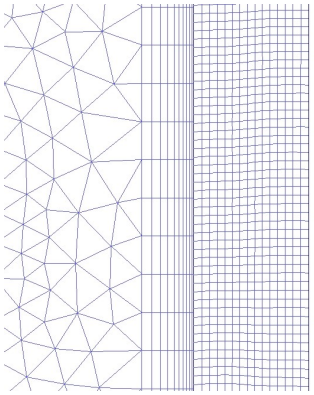

Figure 38: Plywood mesh details on interface.

The walls were named appropriately for applying the boundary conditions (see Table 14):

Symbol	Description
LWB	Bottom left wall;
LWT	Top left wall;
TW	Top wall;
RWT	Top right wall;
RWB	Bottom right wall;
BW	Bottom wall

Table 14: Reference for wall symbols.

Externally, as the experimental apparatus is waterproofed, by foil, and therefore no mass flow (impermeable condition) is considered. Internally, the convective boundary condition is written as:

$$\boldsymbol{g}_v = \upsilon_m \nabla \rho_v + \boldsymbol{u}\rho_v. \tag{63}$$

Table 13 presents the macros used for entering the UDF parameters, while Table 14 shows the symbols used for representing the different plywood box regions.

In Eq. (63), υ_m represents the convective mass transfer coefficient $[m/s]$ and ρ, the vapor specific mass $[kg/m^3]$. In the advection term, $\boldsymbol{u}$ represents the fluid velocity $[m/s]$.

As the supplied air controls the relative humidity inside the plywood box, the moist air is modeled as a species composition of dry air and water vapor. With an initial relative humidity of the air and vapor pressure, the molar fraction of water is calculated as follows:

$$y_w = \frac{P_v}{P_a}, \tag{64}$$

where P_v is vapor pressure $[Pa]$ and P_a represents the atmospheric pressure $[Pa]$. The molar weight of the mixture $M_{(a+v)}$ (dry air and water vapor) is given by:

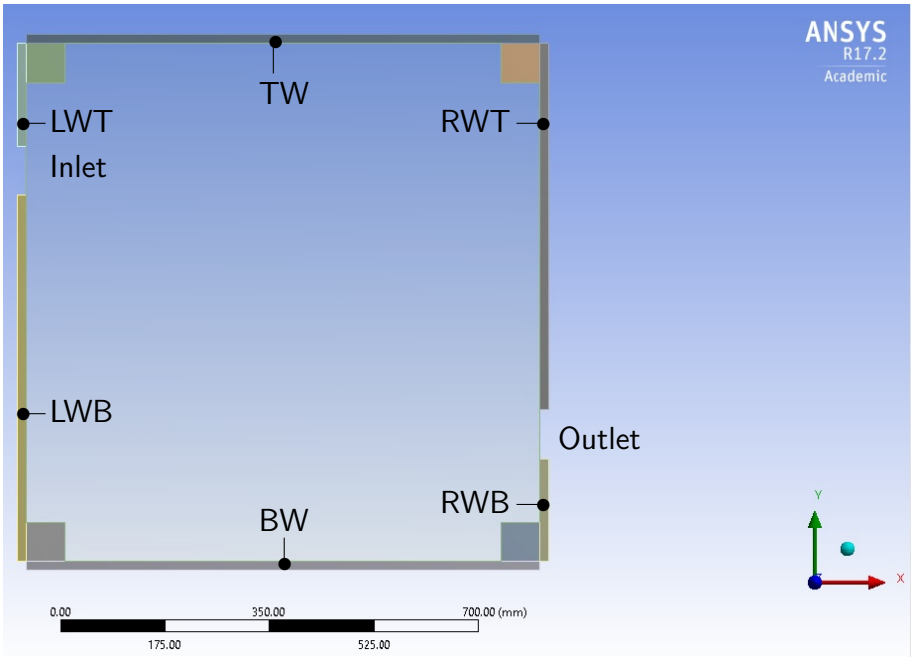

Figure 39: Representation of plywood box in 2D.

$$M_{(a+v)} = y_l M_l + (1 - y_l) M_{dry\ air}, \tag{65}$$

where M represents molar weight. So, the mass fraction of water is represented by:

$$m_l = y_l \frac{M_l}{M_{(a+v)}}. \tag{66}$$

With Eq. (66) the proposed model updates the air relative humidity at the inlet, monitoring the moist air in a simulation according to the experimental.

4.4 Uncertainties

The measurements performed at the laboratory presents some unknown variables regarding plywood properties. It was necessary an investigation after several simulations until to get the appropriate specific mass of the dry-basis material and its vapor permeability function as well. Also, as the moisture stored function was unavailable, it was taken a characteristic model function [11].

Besides of uncertainties about material properties, there is also a risk due to the data acquisition system, including the instrumentation used for measuring relative humidity, temperature and mass [78]. Although isothermal conditions are used to run the experiment, there was a temperature step due to the change in the cycle of the relative humidity. These variations and those related to the thermal inertia of thermocouples have not been taken into account.

Regarding the numerical part, the last simulation [79] used some plywood properties based on published research [81], which may not represent properly the material tested in the laboratory that may be cause some discrepancies between numerical and experimental results. Figure 40 shows some sorption isotherms for plywood, where the water content is represented by mass of moisture absorbed per kg of dry material $[kg/kg]$. Depending on the choice, the results may be not satisfactory as the MBV index is very sensitive to the higroscopicity capacity, which is given by the derivative of the sorption curves. Besides, the omission of liquid transport in the moisture

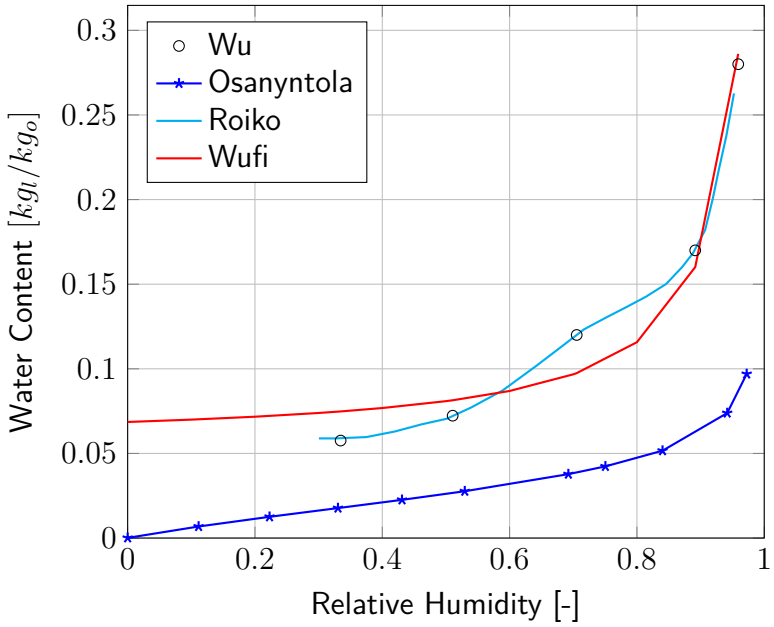

Figure 40: Moisture storage function of plywood.

balance equation contributes to increase those discrepancies. Additionally, the 1-D simulation may not represent well the physical phenomena.

4.5 Material Properties

Some moisture storage functions published in the literature are shown in Fig. 40, and the best curve (suggested by [11]) that describes the plywood moisture behavior in this work is given by:

$$w = \frac{A}{B - \phi} + C. \tag{67}$$

In Eq. (67), ϕ represents the relative humidity RH; A, B and C are constants defined by nonlinear regression according to the measurements made by Wu [82]. Some researchs used Wu measurements as well with an assumption of a fitted-curve represented by cubic interpolation where its derivative is represented by a simple linear function within the range between 30% and 90%. This hypothesis may provide unwarranted results for RH distribution considering the high sensitive to the derivative which is part of the transient term of the moisture conservation equation. For this work, a derivative of Eq. (67) is directly used without any additional function or regression.

Among the curves in Fig. 40, the chosen one (red line) provided better results, allowing even higher time steps (around 900 s for both high and low RH).

The plywood liquid transport $[s]$ coefficient is calculated from [11] and can be written as:

$$D = -D_{ws} \frac{\partial \omega}{\partial \phi} \frac{\phi}{R_v T}, \tag{68}$$

where D_{ws} means moisture diffusion $[m^2/s]$, w, water content $[kg/m^3]$, R_v, an ideal gas constant $[J/(kg \cdot K)]$ for vapor and T, the temperature $[K]$.

With the absence of convection phenomenon in the moisture equation, the vapor diffusion becomes the predominant moisture transport mechanism responsible for the attenuation on the RH

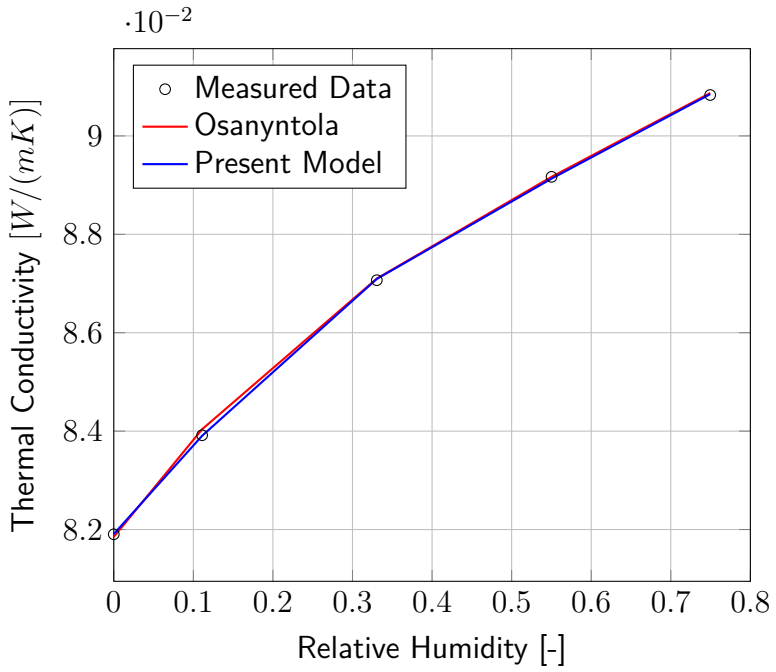

Figure 41: Moisture storage function of plywood.

amplitude in the air domain, due to the sorption/dessorption effects. So, the vapor permeability $[s]$ (suggested by [11]) is obtained by the following relationship:

$$\delta_v = \frac{2 \cdot 10^{-7}}{X} \frac{T^{0.81}}{P_a}, \tag{69}$$

where X means the vapor diffusion parameter which reduction factor of vapor diffusion in air and can be defined as follows [81]:

$$\delta_a = \left(A_1 + \frac{A_2 \phi}{\ln \phi} \right)^{\frac{1}{2}}, \tag{70}$$

where $A_1 = -2.3573 \cdot 10^{-25}$ and $A_2 = -8.1601 \cdot 10^{-24}$; ϕ represents the relative humidity. The proposed model uses Eq. (70) in the moisture equation (Eq. 62a). The effective thermal conductivity of spruce plywood may be described as a polynomial continuous fitted-curve [81]:

$$k_{eff} = \left(A_1 + A_2 \phi + A_3 \phi^2 + A_4 \phi^3 + S \right), \tag{71}$$

where $A_1 = 0.08185$, $A_2 = 0.02212$, $A_3 =$ -0.2313, $A_4 = 0.01291$ and S means the parameter that changes to fit better the curve to the measured data. However, for this work, a new curve provided a better approximation with the measured data:

$$k_{eff} = A_1 \phi^{e^{A_2 \phi}} + A_3 \phi + A_4, \tag{72}$$

where $A_1 =$ 0.254e-2, $A_2 =$ -8.182, $A_3 =$ 0.853e-2 and $A_4 = 0.082$.

Fig. 41 displays the referenced curves to the thermal conductivity $W/(mK)$ of plywood. The density used was 478 kg/m^3 with a specific heat of 1440 $J/(kgK)$.

4.6 Simulation Procedure

The test-cell simulation considers the transient state and, even though is under isothermal condition, the energy conservation equation has also used out in the simulation coupled with the

moisture balance equation. Defined as a boundary condition on the surface, the vapor flux from air to wood panels considers both the convection and diffusion terms (Eq. 63).

The supplied air modeled as an inlet air has its mass fraction calculated to determine the relative humidity of air according to the acquired data.

About time step, an algorithm developed for this work defines it as 3600s, and after that, its value decreases to 900s. These values were chosen to accelerate the simulation and work only without advection term in the moisture flux. Due to the higher non-linearity of convection, the time step had to be reduced to around 1s, which increased substantially the computer run time.

In the simulation, dimensionless numbers such as Reynolds, Prandtl, Schmidt, and Sherwood [72] were calculated to provide the mass and heat transfer convective coefficients at each iteration. In the air zone, an algorithm built for this simulation estimates the vapor pressure and relative humidity.

4.7 Results

The CFD-HAM model has been run considering a test-cell exposed first to 50% of RH during the first 24h. After that, all moisture cycles are taken into account, according to the Nordtest protocol. The objective is to validate the new simulation code and have further information about the air patterns and multi-dimensional distributions of parameters such as the moisture content within the test-cell. For the comparison purposes, both the WUFI, CAR-HAM and, CFD model has been used considering one - and two - dimensional approaches.

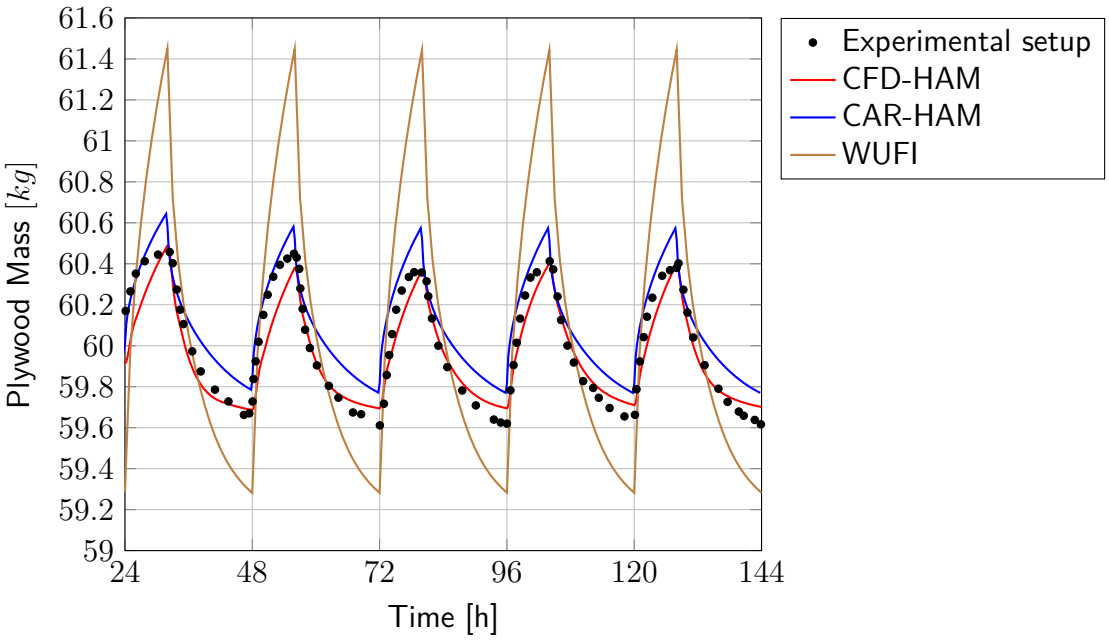

Figure 42: Plywood mass evolution.

In Fig. 42, WUFI software presented unwarranted results likely due to the vapor permeability could not be used for this type of plywood. Additionally, the vapor diffusion depends on the temperature (see Eq. (69)), and for an isothermal condition, the moisture flux becomes constant, which does not happen according to the experimental results. For the 1D simulation, it was considered only the wall thickness, and the boundary conditions employed on the surface guaranted the moisture flux variations according to the changes in relative humidity. The time step used was 3600s, and the computer run time was very short (around 3s). Although the results

had not a good agreement the WUFI software can be used as an initial estimative to know the moisture behavior in the porous media.

In one-dimensional approach, the CAR-HAM model presented good results. In the last three cycles, the average adsorbed mass was 5.3% lower than measured values. For the desorption phase, the difference decreases to 4.2%. Even neglecting the hysteresis and advective effects, the CAR-HAM model provided reliable results. The boundary conditions were set up on the porous material face as a moisture flux led by vapor pressure changes according to the relative humidity measured in the experimental apparatus. This simulation took into account a mesh with only 30 cells, and the run time was 600s.

Both CAR-HAM and WUFI had their convective mass transfer coefficients calculated by the Lewis relation, with heat transfer coefficient $\upsilon_h = 3W/(m^2K)$ (with CFD-HAM model, $\upsilon_h = 2.8W/(m^2K)$).

For the CFD-HAM model, the mass variation in each cycle is lower than the measured data and the stronger hypothesis is that an incorrect vapor permeability. Besides, the moisture storage function may not represent precisely the plywood behavior. Additionally, the hysteresis effect may play an important role on the MBV index. Therefore, an in-depth investigating regarding the plywood properties used in the test-cell could may be reduce those differences. However, the simulated data is very similar for the first 48h. After 24h of stabilization in the chamber, the test-cell adsorbed water until reached almost 60.5kg of mass, which is closer considerably close (less than 0.001 kg) to the 2D model results. On the other hand, the test cell lost more water than what was simulated (48h), with an acceptable result. Between 48h and 72h, the desorption blue line curve shows a good behavior in comparison with Silva [78] experimental data. The last three peaks of the graph are represented very well by the simulation. Other disagreements shown in Fig. 42 are small differences can be considered as irrelevant.

The vapor mass fraction calculated by Eq. (66) enable the amount of water vapor in the air in such a way to achieve the relative humidity cycles in the simulation through the inlet air with a constant velocity. As seen in Fig. 43, some variations in the water vapor mass fraction are noticed when the sorption/desorption starts, showing the delay that calculated values take to fill up the plywood box. The relative humidity of air changed from its initial value of 50% to 75%, kept for 3 hours. After that, RH switches to 33% for 16 hours then the cycle is repeated. It was assumed RH of 15% for the plywood according to the manufacturer's information, where the material RH, for commercial purposes, varies from 5% to 15%. With 32h, the porous material desorbs at 33% of relative humidity. The desorption begins with the majority part of the medium porous filled with water; when low RH phase starts, a capillary pressure becomes higher than the vapor pressure [83] what promotes a liquid migration, Also, the phase-change occurs with liquid evaporation. During desorption, in all cycles, the RH is reduced to 43%; in sorption cycle, this value increases to 70%, except in the first reporting period, where the RH changes from 50% to 62.4%, with an increase of 33%.

Figure 45 shows the relative humidity in the plywood material after 144h of simulation. A higher moisture concentration appears near the corners, where there is a poor air circulation, enable the visualization of fluid movement from the inlet to the outlet.

Figures 46 to 49 present the local mass flow along the wall height. It is noticeable in all moisture flux plots, the peaks with maximum value occur in the same region where vortices appear due to air recirculation near the corners. Near the inlet and outlet zones, the mass exchange is minimum due to the velocities of higher magnitudes in these regions that increases the drying rate.

With the CFD-HAM model, some information regarding simulation is available to analyze the moisture exchange with the plywood, achieving results with confidence. There are some differences in the adsorption phase where the numerical model presents fast adsorption of water

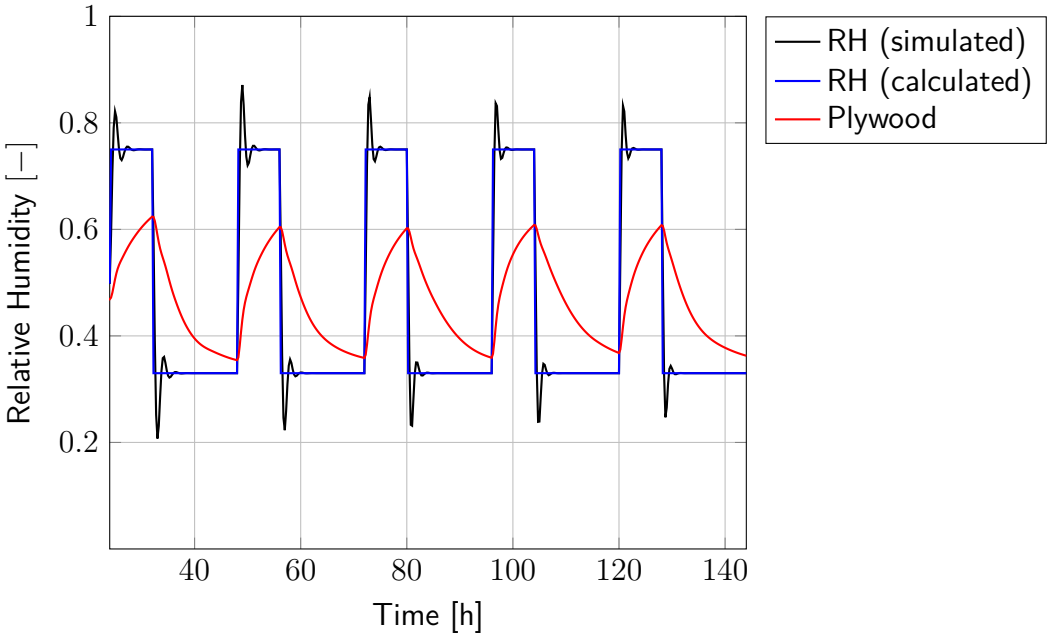

Figure 43: Relative humidity for plywood and air.

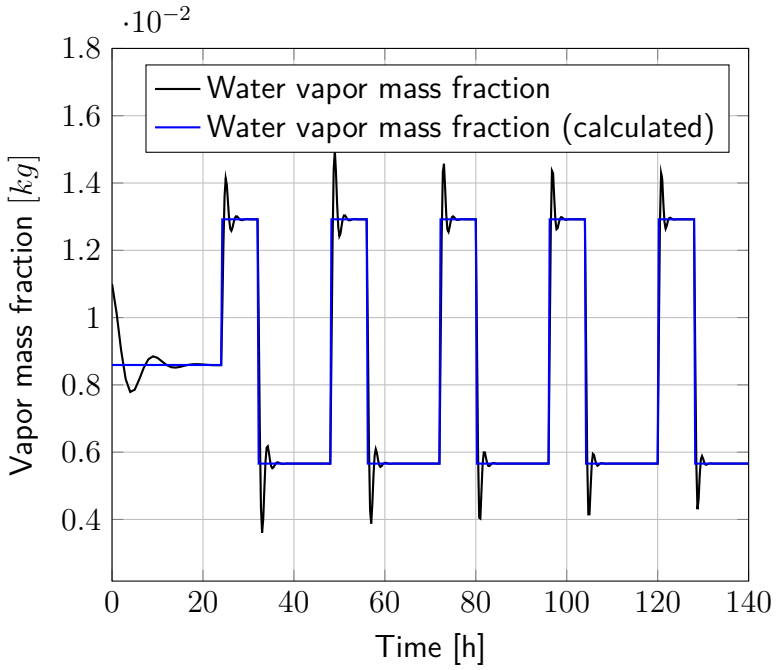

Figure 44: Water vapor mass fraction present in the air.

content, slightly different than the real case; the desorption is very similar to the experimental data. The boundary conditions are applied at the inlet with water mass fraction calculation to assure the correct relative humidity for the surrounding air, where the convective mass and heat transfer coefficients are computed by dimensionless numbers (Reynolds, Prandtl, Schmidt, and Sherwood) provides the mass flow between air and the plywood panels.

With CFD-HAM model use for this case, the computer run time considering two-dimensions took about 8h.

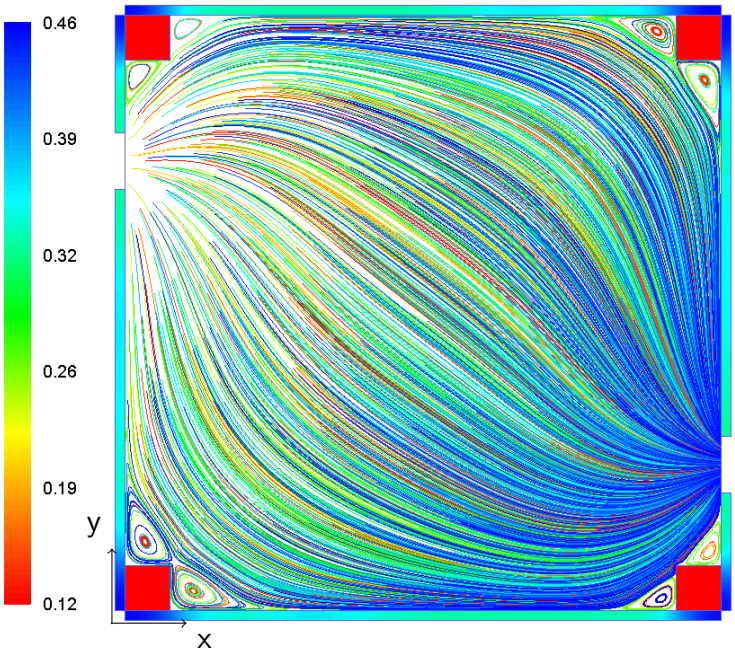

Figure 45: Relative Humidity distribution within the plywood box.

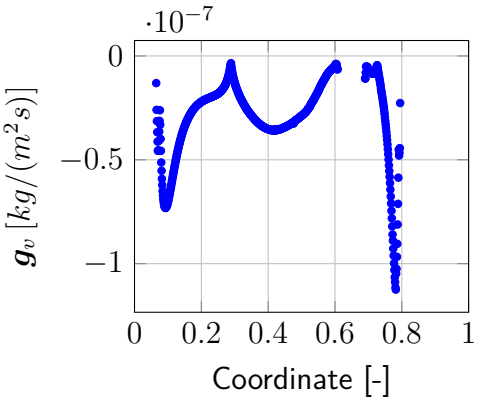

Figure 46: Mass flow along the left wall.

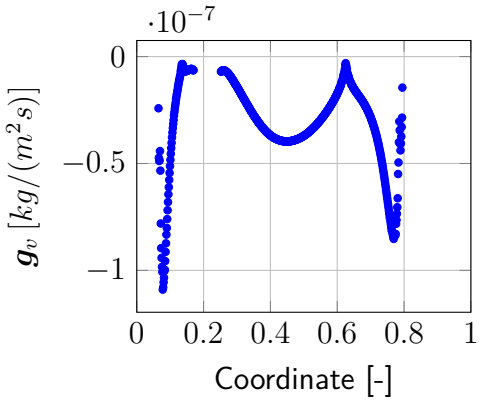

Figure 47: Mass flow along the right wall.

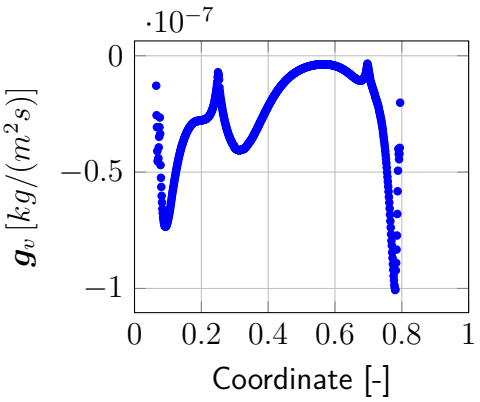

Figure 48: Mass flow along the bottom wall.

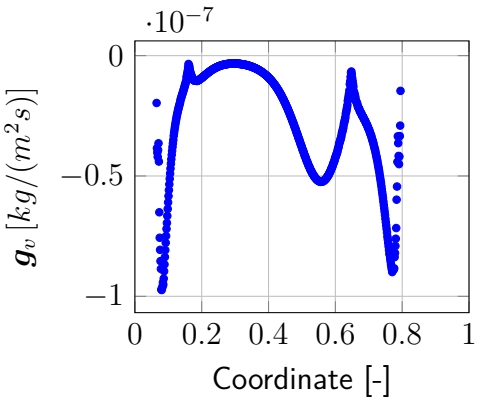

Figure 49: Mass flow along the top wall.

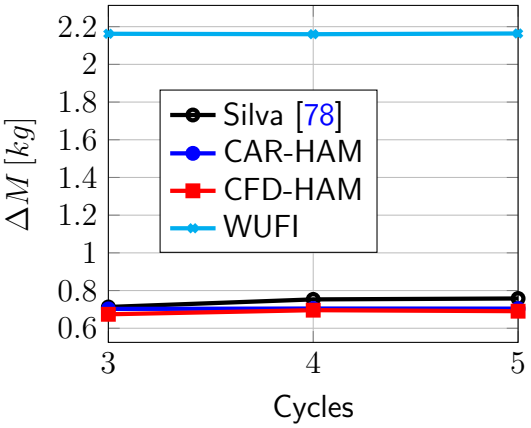

Figure 50: Sorption of water in the last three cycles of simulation.

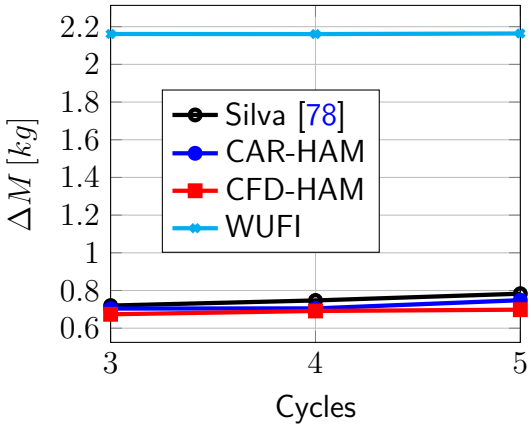

Figure 51: Desorption of water in the last three cycles of simulation.

4.7.1 MBV index

Figures 50 and 51 present the sorption/desorption for each cycle where the CAR-HAM and CFD-HAM models provides the mass variation in good agreement with the measured data of the lab. WUFI software calculated an intensive mass transportation with plywood as the used vapor permeability (Eq. (69)) does not change with relative humidity, which supports the constant values presented in the sorption/desorption curves. Table 15 shows further information about moisture buffer value data over the last three cycles.

	Cycle	Sorption	Desorption	Average	Δ %RH	MBV	Error [%]
Experimental	3	0.71	0.72	0.72	39.10	5.73	
	4	0.75	0.75	0.75	38.40	6.11	
	5	0.76	0.78	0.77	39.96	6.03	
	Average			0.75	39.15	5.96	
CAR-HAM	3	0.67	0.67	0.67	42.00	5.02	12.40
	4	0.70	0.69	0.69	42.00	5.17	15.50
	5	0.69	0.70	0.69	42.00	5.17	14.20
	Average			0.69	42.00	5.12	14.04
CFD-HAM	3	0.70	0.70	0.70	42.00	5.24	8.60
	4	0.70	0.70	0.70	42.00	5.25	14.10
	5	0.70	0.75	0.73	42.00	5.41	10.30
	Average			0.71	42.00	5.30	11.00
WUFI	3	2.16	2.16	2.16	42.00	16.10	180.80
	4	2.16	2.16	2.16	42.00	16.09	163.30
	5	2.16	2.16	2.16	42.00	16.11	167.20
	Average			2.16	42.00	16.10	170.50

Table 15: MBV rating calculation for each simulation code.

In Table 15, the "Sorption" column provides the mass variation $[kg]$ that starts when the relative humidity changes from 33% to 75% and, when its shifted from 75% to 33%, the mass difference is shown in the "Desorption" column. "$\Delta\phi$" is the difference between higher and lower RH (in percent), and finally, "MBV index" column $[kg/(m^2 U_r)]$ exhibits the moisture buffer value calculated according to Eq. (61).nd the last column refers to the error results for each cycle. The first row shows the acquisition data. The second one follows by third one, displays the 1D and

2D models respectively. Wufi results are shown in the last row. Even though the laboratory data be a reference for error calculations, it is noticed at the RH column an data acquisition error in the relative humidity for each cycle. Indeed, the values should be a result of the difference between 75% and 33% of relative humidity (42%) as shown for numerical data simulated by 1D, 2D model and Wufi as well. Due to that, the lower error found in the simulations lies to 2D model with a value of 11%. On the other hand, despising the relative humidity error and considering the same RH variation for the lab. data, the lower error decrease to 4.60%.

The experimental measurements [78] obtained a MBV of 5.95, and the new model (1D and 2D) computed similar values, providing the same rating (see Fig. 36) to the plywood.

4.8 Final remarks

For the simulation of the plywood box under the Nordtest protocol conditions, the proposed model presented similar results found in the laboratory tests. Even with some uncertainties, the simulated data provided reliable results for classifying a porous material according to the MBV index. In the simulations, some moisture storage and vapor permeability functions tested in recently published works and used in this work do not represent with accuracy the material used in the experimental apparatus. The results could certainly be better if the plywood properties had also been measured which is the focus of further research. Additionally, temperature variations in the chamber and in the box may cause some discrepancy not expected by the numerical model. However, for each sorption/desorption cycle, the mass variation of the predicted values and experimental values have an error around 5%.

Regarding run time, WUFI software prooved to be more effective (3s) for a fast prediction of moisture distribution, when compared to the proposed model which has the vapor pressure as a driving potential and deals also with the radiative equation. The CFD-HAM model enables to solve complex problems, but the computer run-time becomes an important issue. To overcome this concern is recommended the use of the CAR-HAM model.

To conclude, the primary purpose of the developed code is to represent well the physical phenomena involving heat and mass transfer in porous media taking into account several hard conditions where the problem can be solved in one, two or three dimensions. Further investigations about computer run-time deserves a profound investigation to bring it to whole-building simulation tools.

4.9 Acknowledgments

The authors acknowledge the Brazilian agencies CAPES, of the Ministry of Education, and CNPq, of the Ministry of Science, Technology and Innovation, for the financial support. The author also acknowledge the ESSS (ESSS Institute for Education, Research and Development) and ANSYS for the technical and research support.

5 General Conclusions

Mathematical models and results on the prediction of distributions of temperature and moisture related variables within porous media were the focus of the present thesis.

First, a new mathematical model formulated for one-dimensional purposes includes – as a novelty – the radiation term, ignored in current models applied to the building simulation field, which can generate wrong results especially for fibrous materials. This code is addressed for fast answers or initial values required for more difficult cases. Then, a multidimensional model is developed for - 2D/3D cases – associated to a CFD software (Ansys-Fluent), enabling complex simulations problems not explored by well-known moisture tools available in literature.

Regarding main equations used in the proposed model, the relative humidity (RH) and temperature have been used for high moisture conditions. Otherwise, vapor pressure potentials replace RH potentials. Some cases well studied in literature were used as references to compare with the model outcomes.

In Chapter 2, the proposed model simulated a drying of a bar under isothermal conditions providing good results where the diffusion phenomenon was more significant, neglecting advection terms. Then, a bar with diffusion and advection phenomena was considered. The advection terms had a relevant role in the moisture distribution, and the air velocity within porous medium was computed in a simple way, being targeted by a difference between indoor and outdoor atmospheric pressure. With the aim to verify the simulation code under hard conditions such as rain load, it was simulated, in a third example, a multilayer wall with high RH, (more than 99%). The driving potentials in the governing equations were set to relative humidity and temperature, providing better results.

For the radiative approach, with the developed CAR-HAM model, the radiative term of governing energy equation was computed by solving the radiative transfer equation (RTE). A residential attic insulation was consider to illustrate the application of the proposed radiative-based model, taking into account the radiative properties of insulation material (with thermal dependency) in an anisotropic medium under the presence of moisture. Clearly, as the thermal conductivities of some insulation materials are very low, the contribution of radiative effect decreases in the building physics domain. However, the same model could be modified and used in the aviation industry or household appliances (ovens and fridges), providing likely a more importante effect of the radiative heat transfer term due to the presence of high temperature gradients.

In Chapter 3, one- and two-dimensional approaches are compared. With the 1D model, the air is approximated to equivalent resistance, with different values from the ones found by the 2D model, which considers the airflow modeled by the Navier-Stokes equations.

In Chapter 4, an experimental test-cell [78] was simulated aiming to get the MBV index [9] of a plywood box. With a 2D sketch, the experimental apparatus was represented with inlet and outlet zones where the internal air was modeled according to the k-ϵ model. The boundary conditions were applied in agreement with laboratory measurements. It was achieved warranted results, even though it could be better with measured material properties.

In general, the proposed model contributes with the complex solution of many problems with heat and mass exchange in porous media under complex conditions and surfaces not represented by current models. The two models presented in Chapters 2 and 3 were verified with published research in literature. Additionally, in Chapter four, the present model is validated with experimental data. In this way, the simulation code proved to be useful, solving problems with mixed conditions involving low and high humidity values and non-uniform convective transfer along surfaces as well.

In addition, with the coupled approach, for each iteration, the heat and mass convective

transfer coefficients are calculated over all surfaces where heat and mass fluxes are needed to solve the distribution of temperature and moisture related variables within the porous domain.

As a drawback, the proposed model may take a significant computer run-time for cases involving fluid flow model, under laminar or turbulent flow regimes. The mesh of surrounding air generates many control volumes which makes the simulation very slow. Another point is the code management. When it is linked to a CFD software, some special user-skills are needed. Even though the Ansys-Fluent has a certain user-friendliness, to load the user defined functions (UDF), the setup of the model needs some previous knowledge of the software.

The code is open to improvements for future research for new implementations such as hysteresis and pollutant presence in the air. With many applications, the hygrothermal model presented in this work could be used for building purposes, help architectures or engineers to develop new buildings, or make retrofit in old buildings. Besides, the developped codes could also support the reverse engineering,to obtain optimized hygrothermal material properties, avoiding damage risks and increase building energy efficiency.

As a future possible investigation not restricted to the building physics area, one could mention the use of the present model to predict vector-borne diseases where the absolute humidity (AH) is a vital index to predict, for instance, dengue incidence. So, with a simulation of surrounding air and walls of the home, the proposed model could provide a moist air behavior and relative humidity content distribution (RH) over entire walls and volume occupied by humans showing the suitable conditions for vector-borne disease spread.

References

[1] U.S. Energy Information Administration. International Energy Outlook, 2017.

[2] European Council and Council of European Union. Energy efficient buildings: increased energy savings and better living conditions, 2017.

[3] W. K. Lewis. The Rate of Drying of Solid Materials. *Journal of Industrial & Engineering Chemistry*, 13(5):427–432, 1921.

[4] D A de Vries. Simultaneous transfer of heat and moisture in porous media. *Transactions, American Geophysical Union*, 39(5):909–916, 1958.

[5] I.E. Chlusov. On the calculation of moisture in roof constructions. In *CIB Conference on Flat Roofs*, Stockholm, 1958.

[6] A.V. Luikov. Heat and Mass Transfer in capillary-porous media. 22:525, 1966.

[7] Marnix Van Belleghem, Marijke Steeman, Arnold Janssens, and Michel De Paepe. Heat, air and moisture transport modelling in ventilated cavity walls. *Journal of Building Physics*, 38(4):317–349, 2014.

[8] Bauklimatik Dresden. Simulation program for the calculation of coupled heat, moisture, air, pollutant, and salt transport., 2011.

[9] Carsten Rode. Workshop on moisture buffer capacity. Technical report, 2003.

[10] D. M. Burch. An Analysis of Moisture Accumulation in Walls Subjected to Hot and Humid Climates. *ASHRAE Transactions*, 93(16):429–439, 1993.

[11] Institute Fraunhofer. WUFI, 2005.

[12] Nathan Mendes. *Models for predicting heat transfer and moisture in porous building components*. Phd's thesis, Federal University of Santa Catarina, 1997.

[13] Nathan Mendes, I. Ridley, Roberto Lamberts, Paulo C Philippi, and K. Budag. Umidus: A PC program for the Prediction of Heat and Mass Transfer in Porous Building Elements. In *International Conference on Building Performance Simulation*, pages 277–283. IBPSA, 1999.

[14] Nathan Mendes, Marx Chhay, Julien Berger, and Dutykh D. *Numerical methods for diffusion phenomena in building physics: a practical introduction*. PUCPRess, Curitiba, 1st edition, 2016.

[15] Pontifical Catholic University - PUCPR. DOMUS software.

[16] Danish Building Research Institute. BSIM - Building Simulation.

[17] I. Fraunhofer. WUFI Plus.

[18] GITHub. ESP-r, 2017.

[19] Drury B Crawley, Linda K Lawrie, Frederick C Winkelmann, and Curtis O Pedersen. Energyplus : New capabilites in a whole-building energy simulation program. pages 51–58, 2001.

[20] Carl-Eric Hagentoft. Determination of liquid water transfer properties of porous building materials and development of numerical assessment methods. Technical Report 960, Chalmers University of Technology, Sweden, 1999.

[21] S Chandrasekhar. *Radiative transfer*. Clarendon Press, Oxford, 1950.

[22] ANSYS. Academic Research, 2017.

[23] Carl Eric Hagentoft, Angela Sasic Kalagasidis, Bijan Adl Zarrabi, Staf Roels, Jan Carmeliet, Hugo Hens, John Grunewald, Max Funk, Rachel Becker, Dina Shamir, Olaf Adan, Harold Brocken, Kumar Kumaran, and Reda Djebbar. Assessment method of numerical prediction models for combined heat, air and moisture transfer in building components: benchmarks for one-dimensional cases. 2004.

[24] S.Y. Harris. *Building Pathology: Deterioration, Diagnostics, and Intervention*. Wiley, New York, 2001.

[25] G.H. Santos and N. Mendes. Numerical analysis of passive cooling using a porous sandy roof. *Applied Thermal Engineering*, 51:25–31, 2013.

[26] V.H.H Gómez and D.M Gálvez. Analytical model for double skin roofs. *Applied Thermal Engineering*, 60:218–224, 2013.

[27] F John. Moisture in buildings. *ASHRAE Journal*, 44:15, 2002.

[28] A.V. Luikov. Heat and mass transfer in capillary-porous bodies. *Advances in Heat Transfer*, 1:123–184, 1964.

[29] C Langlais and S Klarsfeld. Heat and Mass Transfer in Fibrous Insulations. *Journal of Building Physics*, 8(1):49–80, 1984.

[30] Graham W. Jackson and David F. James. The permeability of fibrous porous media. *The Canadian Journal of Chemical Engineering*, 64(3):364–374, 1986.

[31] K Lari and S A Gandjalikhan Nassab. Analysis of Combined Radiative and Conductive Heat Transfer in three-Dimensional Complex Geometries using Blocked-off Method. *IJST - Transactions of Mechanical Engineering*, 35(2):107–119, 2011.

[32] Kaye D Lathrop. Ray effects in discrete ordinate equations. *Nuclear Science and Engineering*, 32(3):357–369, 1968.

[33] J. S. Truelove. Three-dimensional radiation in absorbing-emitting-scattering media using the discrete-ordinates approximation. *Journal of Quantitative Spectroscopy and Radiative Transfer*, 39(1):27–31, 1988.

[34] T.W. Tong and C.L. Tien. Analytical Models for Thermal Radiation in Fibrous Insulations. *Journal of Building Physics*, 4(1):27–44, 1980.

[35] Fatmir Asllanaj, Gérard E. Jeandel, Jean Rodolphe Roche, and David Lacroix. Transient combined radiation and conduction heat transfer in fibrous media with temperature and flux boundary conditions. *International Journal of Thermal Sciences*, 43(10):939–950, 2004.

[36] Kamran Daryabeigi and Transfer Conference. Heat transfer in high temperature fibrous insulation. Number June, pages 1–15, St.Louis,MO, 2002. AIAA/ASME Joint Thermophysics and Heat Transfer Conference.

[37] Anastasios Karamanos, Agis Papadopoulos, and Dimitrios Anastasellos. Heat transfer phenomena in fibrous insulating materials, 2004.

[38] D. Baillis, R. Coquard, and L. M. Moura. Heat transfer in cellulose-based aerogels: Analytical modelling and measurements. *Energy*, 84:732–744, 2015.

[39] Romulo Ruiz Gasparini. *Coupled analysis of heat transfer by conduction and radiation through thermal insulators in residential attics*. Master dissertation, mechanical engineering graduation program, Pontifical Catholic University of Parana, Curitiba, 2005.

[40] Mario A. Medina. On the performance of radiant barriers in combination with different attic insulation levels. *Energy and Buildings*, 33(1):31–40, 2000.

[41] K T. Harris, J A. Roux, and Tyrus Mccarty. Phenolic Binder Content Impact on Total Heat Transfer for Fibrous Insulation Batts. pages 237–257, 2003.

[42] Sandip Mazumder. A New Numerical Procedure for Coupling Radiation in Participating Media With Other. Technical Report September, Ohio State University, Columbus, 2005.

[43] Nathan Mendes, Paulo C Philippi, and Roberto Lamberts. A New Mathematical Model to Solve Highly-Coupled Equations of Heat and Mass Transfer. *International Journal of Heat and Mass Transfer*, 45(3):509–518, 2002.

[44] Nathan Mendes, Paulo C Philippi, and Roberto Lamberts. A Method for Predicting Heat and Moisture Transfer through Multilayered Walls Based on Temperature and Moisture Content Gradients. *International Journal of Heat and Mass Transfer*, 48:37–51, 2005.

[45] Carsten Rode Pedersen. Prediction of Moisture Transfer in Building Constructions. *Building and Environment*, 27(3):387–397, 1992.

[46] Michael F Modest. *Radiative Heat Transfer*. 2013.

[47] L.M Moura. *Identification des propriétés radiatives des matériaux semi-transparents diffuxants en situation de non-symétrie azimutale du camp radiatif.* PhD thesis, Lyon University, 1998.

[48] C J Simonson. Thermal hysteresis in fibrous. *International Journal of Heat and Mass Transfer*, 36:4433–4441, 1993.

[49] Nathan Mendes, F.C. Winkelmann, Roberto Lamberts, and Paulo C Philippi. Moisture Effects on Conduction Loads. *Energy and Buildings*, 35(7):631–644, 2003.

[50] Gerson Henrique dos Santos, Nathan Mendes, and Paulo Cesar Philippi. A building corner model for hygrothermal performance and mould growth risk analyses. *International Journal of Heat and Mass Transfer*, 52(21-22):4862–4872, 2009.

[51] A.W.M. (Jos) van Schijndel and J.L.M. (Jan) Hensen. Integrated Heat, Air and Moisture Modeling Toolkit in MatLab. *Proceedings of the Ninth International IBPSA Conference Montréal, Canada August 15-18, 2005*, pages 1107–1114, 2005.

[52] Marcelo G. Emmel, Marc O. Abadie, and Nathan Mendes. New external convective heat transfer coefficient correlations for isolated low-rise buildings. *Energy and Buildings*, 39(3):335–342, 2007.

[53] W. Mazuroski, N. Mendes, and R.C.L.F Oliveira. Co-Simulation to Bring Advanced Physics to Building Thermal Performance Analysis. In *Proceeding of the Building Simulation Conference*. IBPSA, 2017.

[54] E. Djunaedy, J.L.M. Hensen, and M.G.L.C Loomans. Development of a guideline for selecting a simulation tool for airflow prediction. In *Proceedings of the 8th Int.ernational IBPSA Conference Building Simulation*, pages 267–274. International Building Performance Simulation Association, 2003.

[55] E. Djunaedy. Comparing internal and external run-time coupling of CFD and building energy simulation software. In *Proceedings of the 9th Int. Conf. on Air Distribution in Rooms - ROOMVENT*, pages 393–396, 2004.

[56] E. Djunaedy. *External coupling between building energy simulation and computational fluid dynamics*. PhD thesis, Eindhoven University of Technology, Eindhoven, 2005.

[57] J.L.M. Hensen. A comparison of coupled and decoupled solutions for temperature and air flow in the building. Technical report, University of Strathclyde, Glasgow, UK, 1999.

[58] C. Van Treeck, P. Wenisch, M Borrmann, M. Pfaffinger, M. Egger, and O. Wenisch. Towards interactive thermal confort simulation. In *Proceedings of the European Conference on Computational fluid Dynamics*, Egmond an Zee, 2006. Delft University of Technology; European Comunity on Computational Methods in Applied Sciences (ECCOMAS).

[59] L. Wang and N.H. Wong. Coupled simulations for naturally ventilated rooms between building simulation (BS) and computational fluid dynamics (CFD) for better prediction of indoor thermal environment. *Building and Environment*, 44(1):95–112, 2009.

[60] C. Maliska. Issues on the integration of CFD to building simulation tools. In *Proceedings of the 7th International IBPSA Conference Building Simulation*, pages 29–40. International Building Performance Simulation Association, 2001.

[61] M. Negrão. *Conflation of Computational Fluid Dynamics and Building Thermal Simulation*. PhD thesis, University of Strathclyde, Glasgow, UK, 1995.

[62] Evy Vereecken, H. Janssen, and S. Roels. A determination methodology for the spatial profile of the convective heat transfer coefficient on building components. *Indoor and Built Environment*, 0(0):1–16, 2016.

[63] Evy Vereecken, Kristof Vanoirbeek, and Staf Roels. A preliminary evaluation of mould prediction models based on laboratory experiments. *Energy Procedia*, 78:1407–1412, 2015.

[64] Filip Fedorik, Mikko Malaska, Raimo Hannila, and Antti Haapala. Improving the thermal performance of concrete-sandwich envelopes in relation to the moisture behaviour of building structures in boreal conditions. *Energy and Buildings*, 107:226–233, 2015.

[65] Seong Jin Chang and Sumin Kim. Hygrothermal performance of exterior wall structures using a heat, air and moisture modeling. *Energy Procedia*, 78:3434–3439, 2015.

[66] Krystyna Pietrzyk. A systemic approach to moisture problems in buildings for mould safety modelling. *Building and Environment*, 86, 2015.

[67] Hyeun Jun Moon, Seung Ho Ryu, and Jeong Tai Kim. The effect of moisture transportation on energy efficiency and IAQ in residential buildings. *Energy and Buildings*, 75:439–446, 2014.

[68] Zoltán Sadovsk, Ga Koronthályová, Peter Matiašovsk, and Katarína Mikulová. Probabilistic modelling of mould growth in buildings. *Article Journal of Building Physics*, 37(4):348–366, 2014.

[69] Marnix Van Belleghem. *Modelling coupled heat and moisture transfer between air and porous materials for building applications*. PhD thesis, 2013.

[70] SE Potter and CP Underwood. A modelling method for conjugate heat transfer and fluid flow in building spaces. *Building Services Engineering Research and Technology*, 25(2):111–125, 2004.

[71] Amos Ronzino, Vincenzo Corrado, Maximilian Neusser, and Thomas Bednar. CFD vs lumped model applied to HAM: a comparison between HAM-Tools and Comsol. In *2nd IBPSA-Italy Conference*, pages 491–498, Bozen-Bolzano, 2015. Bozen-Bolzano University Press.

[72] A. Bejan. *Convection Heat Transfer*. John wiley & Sons, New Jersey, third edit edition, 2003.

[73] T Padfield. *The role of absorbent building materials in moderating changes of relative humidity*. PhD thesis, Technical University of Denmark, 1998.

[74] Marc Olivier Abadie and Kátia C Mendonça. Moisture performance of building materials: from material characterization to building simulation using the moisture buffer value concept. *Building and Environment*, 44:388–401, 2009.

[75] T Padfield. Humidity buffering by porous, absorbent insulation and uncertainty about the mechanism of moisture movement in porous absorbent materials. *unpublished paper, National Museum of Denmark, Denmark*, 1999.

[76] Ken-ichi Yoshino, Hiroshi and Mitamura, Teruaki and Hasegawa. *Annex 41 Working meeting, Kyoto*. Kyoto, 2006.

[77] José Walter Meissner, Nathan Mendes, and Kátia C Mendonça. An experimental set-up for evaluating moisture. In *19th International Congress of Mechanical Engineering*, number 2006, Brasilia, DF, 2007. ABCM.

[78] Ayres Siqueira Silva. Análise do método experimental para determinação do índice MBV em materiais higroscópicos, MA Thesis, Mechanical Engineering Graduating Program, Pontifical Catholic University of Parana, 2017.

[79] Guilherme Roiko. Análise numérica da inércia higroscópica em materiais porosos de edificação, MA Thesis, Mechanical Engineering Graduating Program, Pontifical Catholic University of Parana, 2017.

[80] J. W. Meissner, N. Mendes, K. C. Mendonça, and L. M. Moura. A full-scale experimental set-up for evaluating the moisture buffer effects of porous material. *International Communications in Heat and Mass Transfer*, 37(9):1197–1202, 2010.

[81] Olalekan Fatai Osanyintola. *Transient Moisture Characteristics of Spruce Plywood*. PhD thesis, UNiversity of Saskatchewan Saskatoon, 2005.

[82] Yang Wu. *Experimental study of hygrothermal properties for building materials*. PhD thesis, Concordia University, 2007.

[83] C.S Paglarini, F.S Silva, A.G Porti, D. Piasson, and G.F Furtado. Análise da histerese em isotermas de equilíbrio de amêndoas de cumbaru (Dipteryx alata Vogel). *Revista Brasileira de Produtos Agroindustriais*, 15(1):1–6, 2013.